FAILURE DETECTION OF A PSEUDOLITE-BASED REFERENCE SYSTEM USING RESIDUAL MONITORING

THESIS

Michael A. Ciampa, Captain, USAF

AFIT/GE/ENG/09-08

DEPARTMENT OF THE AIR FORCE
AIR UNIVERSITY

AIR FORCE INSTITUTE OF TECHNOLOGY

Wright-Patterson Air Force Base, Ohio

The views expressed in this thesis are those of the author and do not reflect the official policy or position of the United States Air Force, Department of Defense, or the United States Government.

AFIT/GE/ENG/09-08

FAILURE DETECTION OF A PSEUDOLITE-BASED REFERENCE SYSTEM USING RESIDUAL MONITORING

THESIS

Presented to the Faculty

Department of Electrical and Computer Engineering

Graduate School of Engineering and Management

Air Force Institute of Technology

Air University

Air Education and Training Command

In Partial Fulfillment of the Requirements for the

Degree of Master of Science in Electrical Engineering

Michael A. Ciampa, B.S.

Captain, USAF

March 2009

AFIT/GE/ENG/09-08

FAILURE DETECTION OF A PSEUDOLITE-BASED REFERENCE SYSTEM USING RESIDUAL MONITORING

Michael A. Ciampa, B.S.

Captain, USAF

Approved:

Doctor John F. Raquet Thesis Advisor	13 MAR 09 Date
Lt Col Michael J. Veth Committee Member	12 MAR 09 Date
Doctor Meir Pachter Committee Member	13 March 2009 Date

Abstract

The 746th TS uses a flight reference system referred to as the Central Inertial and GPS Test Facility (CIGTF) Reference System (CRS). Currently the CRS is the modern standard flight reference system for navigation testing, but high accuracy is dependent on the availability of GPS. A pseudolite system is currently being developed to augment the CRS and supply the capability to maintain high accuracy navigation under normal and jamming conditions.

Pseudolite measurements typically contain cycle slips and other errors (such as multipath, tropospheric error, measurement noise) that can affect reliability. Past work relied on the receiver-reported signal-to-noise (SNR) value to determine whether or not a cycle slip occurred. However it has been shown that even when the SNR is relatively high, a cycle clip can occur. To reduce the error in the pseudolite measurements, the pseudolite system was integrated with an inertial navigation system (INS). The integrated system detects failures through residual monitoring using a likelihood function. Integrating the inertial sensor provides a means for a filter to maintain the reliability of the pseudolite data which, in turn, increases the integrity of the resulting navigation solution.

An experiment was conducted using six pseudolites and a ground vehicle equipped with a pseudolite receiver, and both a commercial-grade and tactical-grade inertial systems. The inertial data was combined with both real and simulated data to evaluate cycle slip detection performance.

Results from this experiment have shown cycle slips in the carrier phase measurements were detected and corrected using both commercial-grade and tactical-grade INS, but that performance, in terms of probability of detection and time to detect, was improved with the higher quality inertial data.

Acknowledgements

I first and foremost want to thank my family for caring and understanding throughout this endeavor. They were my inspiration during the time I needed it the most. I would also like to thank Dr. Raquet for his guidance and advice through this research. Thank you for taking the time to advise and guide me through this effort.

Michael A. Ciampa

Table of Contents

List of Figures

List of Tables

FAILURE DETECTION OF A PSEUDOLITE-BASED REFERENCE SYSTEM USING RESIDUAL MONITORING

I. Introduction

1.1 Motivation

The development of the Global Positioning System (GPS) has led to improved navigation accuracy over the years. Modern GPS receivers can achieve accuracy on the level of centimeters depending on the processes used to calculate the navigation solution. One issue that has risen with the growth of GPS dependency is the question, "What will happen if GPS is not available?". This question has driven the need for advancement in non-GPS navigation techniques. Depending on the operational environment, there are a number of navigation solutions possible. For a testing environment the highest possible accuracy is desired so that the navigation system being tested is characterized properly. The US Air Force requires the capability to test navigation system with a high level of accuracy, sometimes on the level of a centimeter. Meeting the Air Force's accuracy requirements when testing in a GPS-denied environment has lead to the development of a non-GPS high precision flight reference system, such as a pseudo-satellite reference system.

The 746th Test Squadron at Holloman AFB developed the Central Inertial Guidance Test Facility (CIGTF) Reference System(CRS) for testing aviation-based navigation systems [17]. The CRS is based on a suite of sensors that include a GPS receiver, inertial navigation sensors (INS), an interrogator, and an embedded GPS receiver and INS (EGI). The level of precision the CRS is capable of depends on the availability of GPS measurements. Thus, when testing in a GPS-denied environment the CRS cannot maintain the desired level of centimeter accuracy. When GPS is

denied the CRS relies on the inertial sensors and the interrogator, which can provide accuracy in the order of 1-2 meters.

Recently, the 746th TS have started adding pseudolite measurements to the CRS, augmenting the GPS measurements and enhancing the system during GPS outages. There are still steps needed to advance the pseudolite system so the accuracy can be on par with the current precision of the GPS aided CRS.

Pseudo-satellites, also referred to as pseudolites, are ground-based transmitters that can provide similar navigation measurements as GPS satellites. A pseudolite is a time-of-arrival system that provides range measurements used to calculate position. A pseudolite can operate on a different frequency than the frequencies operated by GPS. This allows the pseudolite system to be used in cases when GPS frequencies are jammed. Past work at Holloman AFB by Raquet et al. [29] has shown the pseudolites can be used as an inverted pseudolite system on an aircraft. An inverted system would be used to track a vehicle using ground stations. Since pseudolites are ground-based an entire network can be modified and changed. This is not possible for an entire GPS constellation, thus pseudolites were used in the development of GPS [24].

Recent research at the Air Force Institute of Technology (AFIT) involving pseudolite navigation has lead to increased accuracy and knowledge about how to improve the ground-based reference system using a pseudolite system developed by Locata Corporation [1] [8] [11] [30]. The prior research discussed different ways in how to reduce the error in the position calculation, when using pseudolite measurements. Constraining the altitude can improve the horizontal position error when using pseudolite measurements [1]. The troposphere error in the measurements can be removed using a model [30]. Survey errors can also be reduced when estimated as part of the navigation filter [30]. There remain other errors in the pseudolite measurements such as multipath fading and cycle slips. Past work has had difficulty detecting the cycle slip errors in the phase measurements.

1.2 Problem Definition

Pseudolite phase measurements can contain cycle slips and slow growing errors. These errors can cause difficulty resolving a navigation solution, due to the randomness that the errors occur. Removing these errors will improve the reliability and accuracy when calculating the pseudolite navigation solution.

1.3 Assumptions

The assumptions made in this research are listed below:

- A real-time navigation solution was not required. The navigation filter was post-processed from stored data.
- Floating point ambiguity estimation is required since integer ambiguity resolution is not possible with the Locata pseudolite system. This is caused by the mechanization of the carrier tracking loop in the Locata receiver.
- The pseudolite transmitter clock error bias is removed through the time lock technique used in Locata's pseudolite system [5].
- The far-near problem with pseudolite systems is handled through the multiple access pulsing technique implemented in the Locata transceivers [5].

1.4 Proposed Solution

Cycle slips and slow growing errors can be detected and removed by using a failure detection algorithm inside a Kalman filter. The navigation filter will consist of integrating a pseudolite system with an inertial navigation system. The inertial system is tightly coupled with the pseudolite measurements to achieve the maximum potential for detecting failures. Single differenced carrier phase measurements will be used to eliminate receiver clock errors. The failure detection algorithm will be designed to detect and remove slow growing errors along with cycle slip errors that occur commonly in pseudolite-based phase measurements.

There are two failure detection algorithms proposed for this effort:

- Algorithm 1 involves using the residual calculated in the Kalman filter during the update portion of the filter algorithm. The likelihood of failure is detected by evaluating the magnitude of the residual relative to the residual standard deviation. This is commonly referred to as "residual monitoring" [20].
- Algorithm 2 implements a moving window as the likelihood function to determine the probability of a failure. The moving window uses the natural logarithm of the probability density function of the residuals over time. The window is made up of N samples, requiring previous information. The natural logarithms of the probability density functions are summed over the course of the window giving the likelihood value. When a failure is present in a measurement the moving window will become more negative. Setting a static threshold is used to detect a failure [20].

1.5 Related Research

1.5.1 Pseudolite-Based Reference Systems. A mobile pseudolite-based reference system, developed by the 746th Test Squadron at Holloman AFB, demonstrated positioning accuracies of $10 - 30$cm [29]. This was a novel approach using an inverted pseudolite design, where the pseudolite was attached to a mobile vehicle and the trajectory was tracked by a network of receivers. This demonstration focused on the use of a ground vehicle as the mobile unit. The pseudolite was observed by multiple non-coplanar receivers strategically laid out to provide good system geometry. Two types of inverted reference systems were demonstrated and compared. The difference between the two systems has to do with the choice of the master transmitter—one used a pseudolite-based reference system and the other used a satellite-based system. The master pseudolite was used as a reference by the other locations in the network of receivers. Both fixed integer and floating point carrier-phase ambiguity resolution was attempted. An iterative batch least squares

algorithm was used to solve for the floating point ambiguities. For this case the floating ambiguity resulted in a more accurate position. This was allocated due to measurement errors and also receiver surveying error [29].

Bouska developed a pseudolite simulation that showed an accuracy of approximately 10-15 centimeters [8]. This work focused on describing and estimating the errors in the pseudolite measurements. In Bouska's simulation, the ambiguities of the pseudolite phase measurements were estimated using a pseudolite only system. The ambiguities were estimated as floating point values.

Ground-based navigation systems have been known to have a deficiency in the vertical geometry. Crawford visualized the vertical geometry of the pseudolite network through the vertical dilution of precision (VDOP) measurements [11]. One way to correct the lapse in vertical geometry would be to use an orbiting pseudolite over the area of interest. This would correct the geometry of the pseudolite network. The vertical position errors can also lead to errors in the horizontal positioning solution [1]. Another technique to correct the vertical issue would be to compensate the vertical channel without changing the geometry of the pseudolite network. Amt developed and implemented five approaches that constrain the vertical channel [1]. The results of this work lead to increased accuracy in the horizontal channel.

Amt demonstrated the position accuracy of the pseudolite-based reference system when using air vehicles [2]. The navigation system was solely based on pseudolite receivers that provided carrier-phase measurements. The position was resolved using a batch least squares algorithm. The least squares method used the pseudoranges to estimate a nominal trajectory for initialization. Then a batch process was used to estimate the ambiguities in the carrier-phase measurement. The ambiguities were resolved using floating point values—this is required for Locata-based carrier phase measurements. The final step of the algorithm presented describes how the carrier-phase measurement is used to resolve position with the estimated ambiguities [1].

Shockley showed the pseudolite system is capable of centimeter level accuracy position determination when unmodeled errors are estimated and mitigated [30] [31]. The errors consisted mostly of a troposphere bias, accounting for 12 centimeters of horizontal position error [30]. The error due to the troposphere is essentially removed through the use of a model based on the current atmospheric conditions and trajectory. The troposphere errors are contained in both the phase and code measurements [30].

Kee et al. showed how the pseudolite signals are subjected to linearization errors when using a first order approximation [10]. The line-of-site vectors are linearized, using a first order Taylor series expansion, as part of the measurement model. This type of measurement model is typically used in a least squares or a Kalman filter-based navigation approach. The GPS signals are also processed in the same manner as the pseudolite measurements, but are subject to less error due to linearization, since the distance of the satellites are much further away from a receiver than the pseudolite-based transmitters [10].

The use of pseudolites as a flight landing system has been studied for the purpose of augmenting current navigation systems to achieve high precision landings [13] [12]. Mostly the pseudolites have been augmented with existing sensors ranging from GPS, GLONASS, barometers, inertial sensors, and radar measurements. One issue with the use of a pseudolite aiding in a landing situation is the ability to lock on to the pseudolite and receive information before the approach. Henzler and Weiser discussed the requirements of a pseudolite system necessary for the use in a flight landing system [13]. Another issue with the pseudolite they used was dealing the near-far problem which is addressed in Section 2.5.3 of this research. Gray and Maybeck focused on the FAA requirements necessary for achieving a precision approach landing using a pseudolite [12]. In their work, it was shown through simulation that the addition of a pseudolite aided in the geometry of the navigation system.

Wang et al. suggested the augmentation of an existing GPS/INS system with a pseudolite for aerial photogrammetry [18]. The inertial sensor was tightly integrated with the pseudolite measurements through an extended Kalman filter. The addition of a pseudolite, to areas where the aerial surveying is being conducted, offered a better geometry then the GPS/INS system alone. The pseudolite measurements were demonstrated to be sensitive to troposphere errors [18].

Lee improved upon existing GPS/INS technology by integrating pseudolite measurements [34]. The results of this work showed the geometry was improved through the addition of a pseudolite. It was noted the pseudolite contained large residual errors due to multipath [34].

1.5.2 Locata Pseudolites. Locata Corporation developed a pseudolite-based reference system that offers new capabilities by solving the majority of the issues previously mentioned, including the near-far problem, transmitter time bias, and multipath effects. Additionally, the Locata pseudolites operate at a non-GPS frequency, so they are ideal for situations in which GPS frequencies are denied. Barnes et al. discussed the benefits of the Locata system [5] [4] [6]. The Locata system resolved the timing issues using a TimeLoc technique that synchronizes the transceivers to one master clock [6]. The Locata-based system has been developed to achieve centimeter level accuracy [4], similar to the accuracy level of carrier phase differential GPS. Also, this system has been used indoors with an accuracy of 20cm and less in a kinematic experiment [5].

1.5.3 Pseudolite-Based Navigation for Indoors and Urban Canyons. Wang et al. expanded on an existing GPS/INS-based navigation system by integrating with pseudolite-based measurements to improve the geometry of the GPS system in the case of an urban canyon [35]. An urban canyon is when the buildings in a large city render the GPS signals useless through either reflecting the signals or completely blocking the signals. Adding pseudolites in an environment like this can add to the

geometry and decrease the number of required GPS signals necessary to solve for a position solution [35].

Indoor use of pseudolites for navigation has been shown to be possible, but is subject to large amounts of multipath fading when used in a standalone configuration [3] [28] [16]. Adding an INS to aid in the pseudolite receiver can help mitigate the multipath effects. The work in [3] has shown the use of ultra tight integration improves the use of pseudolites for indoor navigation. Also suggested in this work is the use of a medium quality inertial sensor (1 deg/hr gyro bias and 10 milli-g accelerometer bias) in place of a low quality inertial sensor. Multipath can be mitigated inside the frequency lock loop in the receiver through the use of a fading channel model [15]. The indoor fading model uses the filter estimates inside the receiver to aid in rejecting multipath.

Petrovski et al. focused on indoor navigation with a standalone pseudolite system [28]. They focused on resolving the initial position using the pseudoranges and also resolved the ambiguities inside of the filter. The algorithm presented was designed after similar GPS ambiguity estimation techniques. Kao also presents another relative motion ambiguity estimation technique for indoor navigation [16]. The difference in this work is the pseudolites have been tightly integrated with inertial measurements for improvement of indoor navigation. The inertial measurements aid in the ambiguity estimation of the carrier phase.

1.5.4 GPS/INS Integration. Zhang et al. presented the comparison of the HG1700 and the LN200 inertial sensors aided by kinematic differential GPS [37]. The position error of dead reckoning navigation was analyzed with the two inertial sensors and showed the position error will grow to 10cm for a 2 second outage time using the HG1700. The LN200 can hold the error to less than 10cm for up to a 4 second outage. The difference in inertial sensors becomes more apparent as the outage times become longer. The HG1700 reaches 1.8 meters in error with a 26

second of outage, while the LN200 can have an outage for 40 seconds for the same error [37].

Petovello presented the benefits of tight inertial integration with GPS measurements over loose integration when estimating floating point ambiguities [27]. The tightly coupled system resolved the ambiguities faster and more accurately than the loosely coupled or the GPS-only system. This became more obvious as GPS outages became longer. In the case of a 40 second outage, the tightly coupled system yielded a 10cm improvement over the loosely coupled version. The work also showed the increased reliability when using an integrated system over a GPS-only method.

1.5.4.1 Reliability Testing. Petovello discussed the integration of GPS with an inertial navigation system [26]. The inertial system is used to improve the reliability in the system through failure detection. Petovello also discussed the tradeoffs of using a tightly coupled inertial model vice a loosely couple or ultra-tight integration. Reliability is used to assure the quality of the observation inside a Kalman filter. A more complete statistical reliability, using GPS measurements, was developed to work in conjunction with a Kalman filter [25] [26]. Statistical reliability provides a method to detect if a measurement is error free. Having the ability to detect errors in the measurements could prevent the Kalman filter state estimates from becoming corrupted. Statistical reliability uses the measurement covariance to analyze the measurement errors and not the observations directly. Because of this, the internal reliability can be shown to increase as the measurement updates are processed, and thus the state covariance reduces in uncertainty. The resulting error statistic from the internal reliability test is referred to as the Minimum Detectable Blunder (MDB). The MDB is based on the geometry of the system, measurement covariance, process noise, and covariance of the state estimates. The MDB is then propagated to calculate the error in the state estimates caused by the undetected errors, described as an external reliability test. The resulting statistic was referred to as the protection level. The protection level can be used as a threshold to detect when

the state vector is no longer an accurate estimate. Wieser et al. also implemented this failure detection algorithm, described in [26], using a real-time kinematic GPS and INS system [36]. Wieser's work focused on failure detection, identification, and model adaptation. The likelihood ratio was used in this work to test possible failure scenarios.

1.5.5 Residual Monitoring. An integrity monitoring algorithm known as Autonomous Integrity Monitored Extrapolation (AIME) has been shown to provide 99.999% continuity when no GPS signals are available [14]. FAA requirements for precision landings were the driving force behind the development of this algorithm. AIME has been developed to use all the information from the sensors onboard an aircraft. AIME has been shown to detect multiple failures simultaneously. AIME was used to detect multiple satellite failures by using an independent inertial-based navigation system. The algorithm specializes in detecting errors that quickly decorrelate over time (two minutes or less), versus slowly decorrelating errors. This is because AIME uses an independent inertial navigation system (INS) to compare with the navigation solution and in turn determines when an error is present in an observation. To keep the INS independent the measurements are saved over some period of time before the INS is updated allowing the measurements to be verified, thus preventing the filter from becoming corrupted. The AIME algorithm distributes the averaged residuals using a chi square test with n degrees of freedom, where n is equal to the number of GPS satellites current in the observation [14].

Another error detection algorithm is known as the rate detector algorithm, developed by Umar Bhatti [7]. This algorithm is an integrity monitor based on the rate of change of the residual errors in the Kalman filter. The algorithm focuses on detecting the slope of the growing errors, which are referred to as test statistics. The test statistics are derived from analyzing the changes in the residuals. This work is derived from two other integrity monitoring techniques commonly used—GPS integrity channel, and Receiver Autonomous Integrity Monitoring (RAIM).

The rate detector algorithm is based on an external aiding by an inertial navigation system. This monitoring technique was developed to be used in conjunction with Micro Electro Mechanical Systems (MEMs) inertial sensors. The algorithm was integrated by using an INS tightly coupled with GPS measurements. This algorithm has been simulated to show a capability to detect slow growing errors, specifically focusing on slow growing errors in GPS pseudorange measurements [7].

1.6 Thesis Overview

Chapter 2 presents the background information used to develop and implement the failure detection algorithm. This consists of a detailed explanation of the Kalman filter equations, modeling of pseudolite measurements and the basics of inertial navigation. The last section will discuss the basis of failure detection in a Kalman filter.

Chapter 3 shows the development and implementation of the navigation reference system. The navigation filter is developed as an error state extended Kalman filter. The filter is present in two sections; the first discusses the INS error model used in the filter. While the second section focuses on the pseudolite measurement model. The chapter finishes with a discussion on the failure detection implementation and how the field experiment and simulation were accomplished.

Chapter 4 presents the results of the failure detection algorithm, based on the field experiment and simulations. A comparison of inertial sensors is shown in detail focusing on the statistics of failure detections. The results of both failure detection algorithms are compared in terms of detection rate, detection delay, and false alarms.

Chapter 5 concludes the results of the failure detection algorithms and the impact the quality of inertial measurements has in the detection of errors. Finally enhancements to the failure detection algorithms are offered along with future efforts to expand on this research.

II. Background

This chapter presents the background information that will be used to develop the navigation filter and failure detection algorithm. The inertial sensor mechanization will be discussed in detail. The Global Positioning System (GPS) will be presented to describe the basis of the pseudolite navigation system. The Kalman filter will be described while presenting the algorithm for the regular Kalman filter and the extended Kalman filter. Finally, the idea of failure detection and previous methods used with the Kalman filter will be described.

2.1 Reference Frames

Reference frames are used to describe the vehicles position, velocity, and attitude as it navigates along a trajectory. Inertial navigation is based on Newton's laws of motion which are approximated in the inertial frame. Mechanization of the inertial measurements requires knowledge of the body frame and local navigation frame in addition to the inertial frame. The pseudolite measurements are used to calculate a position in the local navigation frame. The positions of the pseudolites are known in the Earth centered Earth fixed frame. The reference frames described below and shown in Figure 2.1 are presented with more detail in [32].

2.1.1 Earth Centered Earth Fixed Frame. The Earth centered Earth fixed frame (ECEF) has an origin at the center of the Earth. The z-axis points out the North Pole and the x-axis extends through where the Greenwich meridian and the equator intersect. The ECEF frame is fixed to the Earth, thus it rotates with Earth.

2.1.2 Inertial Frame. The origin of the inertial frame (i-frame) is co-located with the ECEF frame at the Earth's center. The z-axis of the i-frame also extends through the North Pole (spin axis). But unlike the ECEF frame, the i-frame is a fixed frame that does not rotate with Earth. The x^i-axis points towards the first

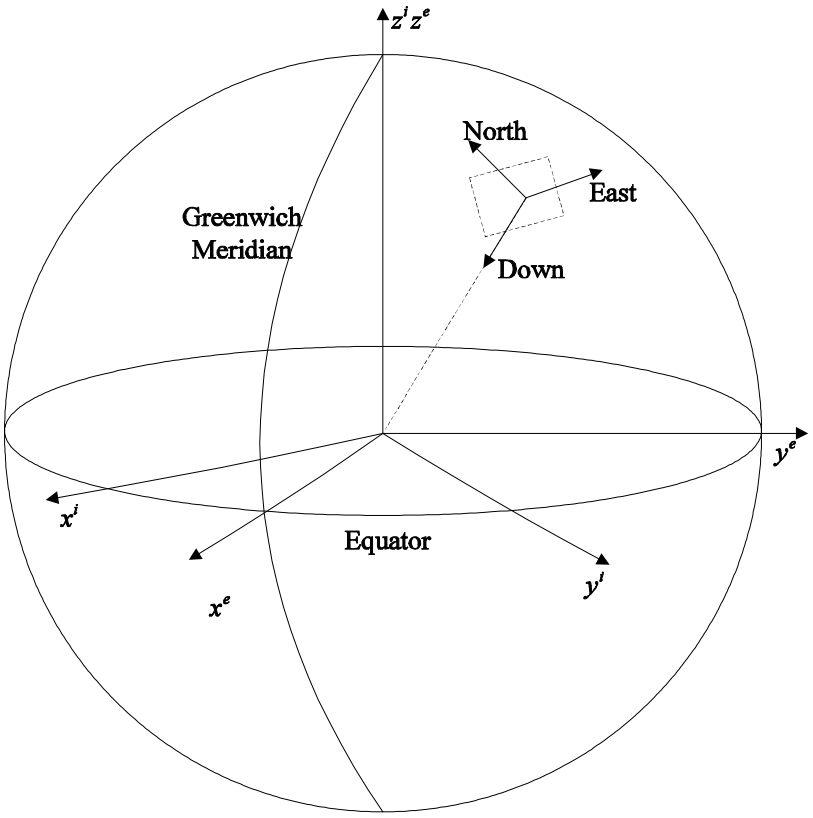

Figure 2.1: The Reference Frames are shown in Comparison to Each Other and Earth.

star in Aries. The inertial frame is where Newton's laws are approximately defined thus this is where the inertial measurements exist.

2.1.3 Body Frame. The body frame is used to reference the vehicle of interest. The origin is located at the center of the vehicle with the x-axis pointing out the front, the y-axis is pointing out the right of the craft, and the z-axis is pointing down, shown in Figure 2.2. This frame also defines the roll, pitch and yaw of the craft.

2.1.4 World Geodetic System 84 (WGS84). The world geodetic system is used to define coordinates in latitude, longitude, and altitude. WGS84 is not a fixed axis system such as the frames discussed above. The WGS84 is a datum used to calculate the coordinates from a known ECEF position.

2.1.5 Local Geographic. This category of reference frames includes local coordinates such as the East, North, Up Frame (ENU) and the North, East, Down Frame (NED). This type of reference frame is commonly referred to as the navigation frame. The NED frame is shown in Figure 2.1.

2.1.6 Reference Frame Conversions. Each of the frames are necessary to describe the multiple sensors in a navigation system. When a number of reference frames and coordinate systems are implemented in the same navigation system the need to convert between references is necessary. The following is an example of a navigation system that contains an inertial sensor, GPS and pseudolites. The inertial system measurements come from the inertial frame. The inertial system is then mechanized into the NED frame. On the other hand GPS and pseudolite measurements are derived in the ECEF frame and typically expressed in the ENU frame or WGS84 coordinates.

To transform between two frames a rotation (and sometimes translation) is required. This is true when converting between the ECEF, ENU, and NED frames.

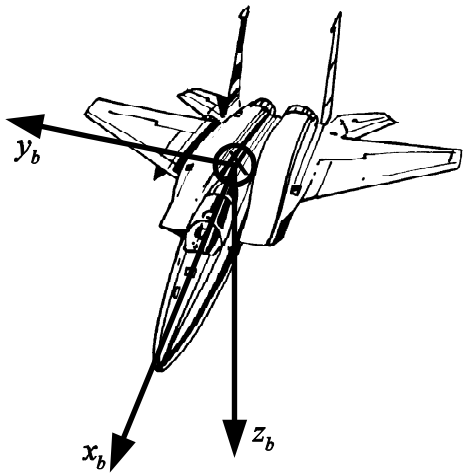

Figure 2.2: The Body Reference Frame, Located Within the Vehicle.

The rotation from one frame to another is accomplished by using a direction cosine matrix (DCM).

2.2 Inertial Navigation System

An inertial measurement unit (IMU) is a device used in navigation to solve for the position, velocity, and attitude in a self-contained passive sensor. IMUs are constructed using two types of sensors—gyroscopes and accelerometers. To observe three dimensions of translation and rotation three of each type of sensors are packaged together to make an inertial measurement unit. Strapdown inertial systems are commonly used today, since they tend to be smaller and more reliable than other types of inertial systems. A strapdown system includes IMUs rigidly attached to the body of the object in interest. A strapdown system allows the inertial system to rotate with the body frame and around the local navigation reference frame. Platform systems are also used less commonly on systems today. A platform system is stabilized in the local navigation reference frame or some other defined reference frame, does not rotate with the body frame, using gimbals, similar to how a compass

works. This technique is used less frequently now since it requires a large amount of maintenance and typically results in a larger, more complicated system.

The gyroscopes in an IMU measure the angular rate from the inertial frame to the body frame. A single gyroscope measures the angular motion around one axis. Thus there are three gyroscopes aligned orthogonally to each other. The result from integrating the data from the gyro yields the Euler angles describing the attitude of the object. The angular body rate with respect to the navigation frame (ω_{nb}^{b}) is found from the difference of the body rate measured by the IMU with respect to the inertial frame (ω_{ib}^{b}) and the estimated Earth rate expressed in the navigation frame with respect to the inertial frame (ω_{in}^{n}), transformed using the navigation to body transformation matrix (C_{n}^{b}), Equation (2.1).

$$\omega_{nb}^{b} = \omega_{ib}^{b} - C_{n}^{b}\omega_{in}^{n} \tag{2.1}$$

Accelerometers, despite their namesake, measure specific force in the body frame and not the acceleration directly. To find acceleration, in the i-frame, (a^i) form the output of an accelerometer, a gravity model is needed to remove the gravity component (g^i) from the specific force (f^i).

$$a^i = f^i + g^i = C_b^i f^b + g^i \tag{2.2}$$

where C_b^i is the body frame to the i-frame transformation matrix [32].

The WGS-84 gravitational model [22] is commonly used to model the gravity in navigation systems. The inputs to the gravitational model are latitude, longitude and height above ellipsoid. The output of the accelerometers when integrated results in the velocity of the object. A second integration resolves the position. Together the accelerometers and the gyroscope can give valuable information of where the object is currently, its current velocity, and the attitude of the object.

Inertial navigation systems are susceptible to drift over time. The drifts corrupt the acceleration and angular rate measurements. They are inherent to every inertial sensor. The size of the drift can be reduced depending on the type of inertial system. Drift is caused by white noise inside the raw measurements. Along with a drift, inertial systems can also be subject to a constant turn on bias.

If the gravity component is not removed completely a navigation system can drift in any axis in the navigation frame. This is typically caused by removing to little or too much of the gravity parameter from the accelerometer using Equation (2.2). This error is caused by a difference from the estimated gravity from the model to the actual gravity. To reduce this error an inertial navigation system can be integrated with an altimeter to resolve the error in the z-axis of the navigation frame.

Inertial navigation systems come in many different shapes and sizes and depending on the error allowable in the system being designed the proper INS can be chosen. Large airplanes typically use advanced ring laser inertial systems known as navigation grade systems. This type of INS has an angular drift error of approximately 0.01 deg/hr. Tactical grade inertial systems are typically found on systems that only need to use a navigation system for a short time (several minutes) or do not require the precision of a navigation grade system. Tactical grade IMUs have a drift on the order of 1 deg/hr. Another class of IMUs is known as commercial grade. These exhibit a drift rate of 10+ deg/hr. This error is highly undesirable but the commercial grade is fairly inexpensive.

2.2.1 Inertial Navigation Implementation. The mechanization model, in the local level navigation frame, using inertial data is depicted in Figure 2.3. Developing a model allows the opportunity to implement error modeling. An error model of an IMU is important since the drift errors and bias need to be described and removed from the IMU. Also a model allows for the inertial measurements to be integrated with other means of navigating such as GPS.

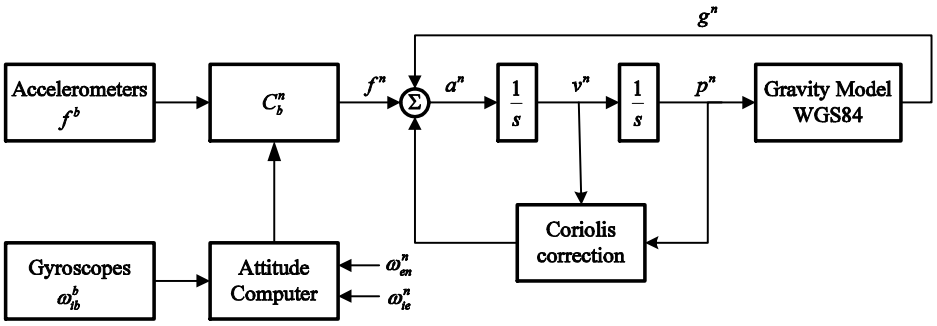

Figure 2.3: The Inertial Mechanization Model shown for the Local Level Frame.

The first step when working with inertial measurements is to remove the biases from the accelerometer, f_{ins}^b, and gyroscope, $\omega_{ib_{ins}}^b$, measurements as shown in Equation (2.3) and (2.4). The raw inertial measurements contain white Gaussian noise, w_{ins}^f and w_{ins}^ω.

$$f_{ins}^b = f^b + a_{bias} + \mathrm{w}_{ins}^f \tag{2.3}$$

$$\omega_{ib_{ins}}^b = \omega_{ib}^b + \omega_{bias} + \mathrm{w}_{ins}^\omega \tag{2.4}$$

A bias can be modeled as a constant or a drift. If modeled as a constant, the bias can be removed for an entire data set by calculating the average error over period of time when there is no motion, such as an alignment period. However the bias will drift over time. The amount of drift depends on the type of IMU being used and the length of navigation. For a more accurate model the bias can estimated as a drift, shown as a_{bias} and ω_{bias}. The drift is modeled as a first order Gauss-Markov process [33], driven by white Gaussian noise, w_{bias}^a, shown in Equation (2.5). This model allows the biases to be estimated inside a Kalman filter.

$$\dot{a}_{bias} = -\frac{a_{bias}}{T} + \mathrm{w}_{bias}^a \tag{2.5}$$

where T is the time constant.

The strapdown mechanization for raw inertial data is described in Figure 2.3 [32]. It is required that the attitude be calculated prior to being able to resolve

the accelerometer measurements into the navigation frame. This is done by the attitude computer using the gyro data to calculate the change in attitude from the last known point. The attitude computer in the IMU mechanization calculates the transformation matrix (C_b^n). Also the attitude computer requires the initial description of the attitude and position of the object.

$$\dot{C}_b^n = C_b^n \Omega_{nb}^b \tag{2.6}$$

where C_b^n is the body to navigation frame rotation matrix and Ω_{nb}^b is the skew symmetric matrix

$$\Omega_{nb}^b = \begin{bmatrix} 0 & -\omega_z & \omega_y \\ \omega_z & 0 & -\omega_x \\ -\omega_y & \omega_x & 0 \end{bmatrix} \tag{2.7}$$

where ω_x, ω_x, and ω_x are the angular rates around the x, y, and z axes. Since inertial measurements are discrete, a difference equation can be used to calculate the direction cosine matrix (DCM) at $t + \delta t$. Equation (2.8) is only valid when the change in angle is relatively small.

$$C_b^n(t + \delta t) = C_b^n(t)[I_{3x3} + \delta\Psi] \tag{2.8}$$

where

$$\delta\Psi = \begin{bmatrix} 0 & -\delta\psi & \delta\theta \\ \delta\psi & 0 & -\delta\phi \\ -\delta\theta & \delta\phi & 0 \end{bmatrix} \tag{2.9}$$

The variables $\delta\phi$, $\delta\theta$, and $\delta\psi$ represent the body rates as measured by the gyroscopes from time t to time $t + \delta t$.

The next step is to use the heading information just calculated to rotate the inertial measurements from the body frame to the navigation frame. Also since the accelerometer is reading specific force and not acceleration, the gravity term will also

need to be removed at this step, as given by

$$a^n = C_b^n f^b - [2\omega_{ie}^n + \omega_{en}^n] \times v_e^n + g^n \tag{2.10}$$

where ω_{ie}^n is the Earth turn rate with respect to the navigation frame, ω_{en}^n is the rate of turn of the navigation frame with respect to the Earth frame, and v_e^n is the ground speed expressed in the navigation frame. The coriolis term will be removed next. The coriolis effect is when in the inertial frame of reference the flight path appears to be a straight line, but in the Earth frame the flight path appears to curve. The coriolis correction compensates the flight path to the Earth rotation rate in respect to the navigation frame.

At this point the raw accelerations (a^n) are integrated once for velocity (v^n), and again to calculate position (p^n). An inertial sensor requires knowledge of the starting location. Without an initial velocity or position the accelerometer cannot be mechanized to solve the navigation solution.

2.3 Global Positioning System

The Global Positioning System (GPS) is made up of a constellation of satellites that transmit signals used for navigation and timing. GPS is known as a time-of-arrival (TOA) system, meaning that the range of the signal is calculated based on the time it was received. The transmit time is contained in the navigation message of the signal transmitted. Since the satellite clock and receiver clock are not synchronized, there will be errors based on the timing in a GPS range, so this type of measurement is referred to as a pseudorange. GPS satellites are identified by the unique pseudorandom noise (PRN) they transmit.

GPS currently operates on two different carrier frequencies, L1 (1575.42 MHz) and L2 (1227.6 MHz). The future system will include a third frequency referred to as L5. The GPS constellation is made up of between 24 to 30 satellites.

GPS provides three measurements that can be used in a receiver to compute navigation information. These measurements include Doppler, carrier phase, and pseudorange measurements. There is a fourth measurement when using a GPS system called carrier-to-noise density, but is used to determine the quality of the measurements from a specific PRN. The carrier-to-noise density, C/N_0, is the relative power from one satellite to receiver. Pseudoranges alone provide a navigation accuracy of about 10 meters. When carrier phase measurements are used for positioning, they can provide an accuracy of 10cm and better. To achieve carrier phase navigation, ambiguities will need to be resolved. This can be done in many ways but typically the pseudoranges are used to initialize the ambiguities in the least squares solution or the Kalman filter solution. Over time the residual errors are used to resolve the ambiguities to fixed integers [21].

The pseudorange measurements for GPS contain errors from multiple sources, shown in Equation (2.11).

$$\rho = r + T + \frac{I}{f^2} + c\delta t_{rec} - c\delta t_{sv} + v_\rho + m_\rho \tag{2.11}$$

where

$$\begin{aligned}
r &= \text{true range measurement (meters)} \\
T &= \text{tropospheric delay (meters)} \\
\frac{I}{f^2} &= \text{ionospheric delay (meters)} \\
c\delta t_{rec} &= \text{clock error due to receiver (meters)} \\
c\delta t_{sv} &= \text{clock error due to satellite (meters)} \\
v &= \text{measurement noise (meters)} \\
m &= \text{multipath error (meters)}
\end{aligned}$$

The carrier phase measurement for GPS is much more accurate then the code but can be difficult to use since the ambiguities, N, are unknown. Even when the ambiguities are resolved they can still suffer from cycle slips. The ambiguities in a GPS system are fixed integers. The carrier phase is modeled as

$$\phi = \frac{1}{\lambda}(r + c\delta t_{rec} - c\delta t_{sv} + T - \frac{I}{f^2} + v_\phi + m_\phi) + N \tag{2.12}$$

where λ is the wavelength of the carrier and N is the ambiguity (cycles). The Doppler measurement is the derivative of the carrier phase. The Doppler can be used to calculated velocity relative to the satellite.

2.3.1 Differential GPS. Differential GPS is used to reduce common errors in GPS measurements. There are two commonly used DGPS techniques—the first is single differencing the measurement and the second is double differencing the GPS measurements.

A single difference GPS measurement uses one satellite and two receivers, with one receiver being a reference receiver at a known location. Single differencing is done to remove common errors such as satellite clock error. A single difference GPS measurement scenario is depicted in Figure 2.4. Single differencing also reduces the error contributed by the ephemeris, ionosphere, and troposphere. However the amount of error that is canceled in the difference depends on the baseline distance between the two receivers. For a short baseline, the atmosphere and ephemeris errors can essentially be cancelled out using single differencing [21]. The definition of a short distance in terms of baseline can vary depending on the atmosphere effects [21]. The single difference pseudorange measurement is represented as

$$\triangle\rho^A_{1,2} = \rho^A_1 - \rho^A_2 = r^A_{1,2} + T^A_{1,2} + \frac{I^A_{1,2}}{f^2} + c\delta t_{1,2} + v^A_{1,2} + m^A_{1,2} \tag{2.13}$$

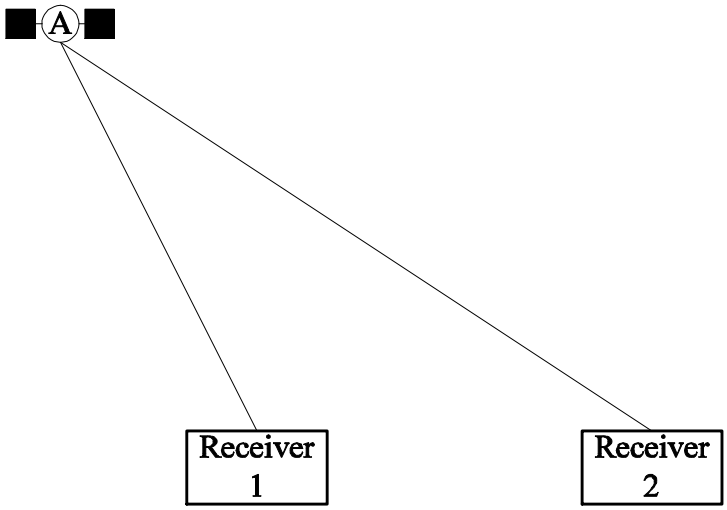

Figure 2.4: Example of Single Differenced GPS Measurements.

The corresponding single difference phase measurement is represented as

$$\triangle\phi_{1,2}^{A} = \phi_{1}^{A} - \phi_{2}^{A} = \frac{1}{\lambda}(r_{1,2}^{A} + c\delta t_{1,2} + T_{1,2}^{A} - \frac{I_{12}^{A}}{f^2} + v_{1,2}^{A} + m_{1,2}^{A}) + \Delta N_{1,2}^{A} \qquad (2.14)$$

Double differencing the measurements is used to remove the clock error in the receiver. Double difference GPS measurements require two satellites as shown in Figure 2.5. The single difference measurements calculated previously are now subtracted from each other. The double difference pseudorange is calculated using the single difference Equation (2.13). The resulting double difference equation is

$$\bigtriangledown \triangle \rho_{1,2}^{A,B} = \triangle\rho_{1,2}^{A} - \triangle\rho_{1,2}^{B} = r_{1,2}^{A,B} + T_{1,2}^{A,B} + \frac{I_{1,2}^{A,B}}{f^2} + v_{1,2}^{A,B} + m_{1,2}^{A,B} \qquad (2.15)$$

and the double difference carrier phase measurement becomes

$$\bigtriangledown\triangle\phi_{1,2}^{A,B} = \triangle\phi_{1,2}^{A} - \triangle\phi_{1,2}^{B} = \frac{1}{\lambda}(r_{1,2}^{A,B} + T_{1,2}^{A,B} - \frac{I_{1,2}^{A,B}}{f^2} + v_{1,2}^{A,B} + m_{1,2}^{A,B}) + \bigtriangledown\triangle N_{1,2}^{A,B} \quad (2.16)$$

The ambiguity for both the single difference and double difference is still maintained as a fixed integer.

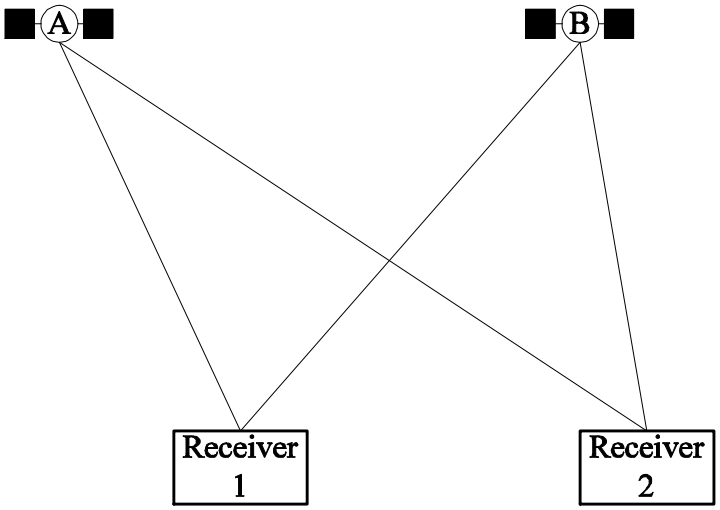

Figure 2.5: Example of Double Differenced GPS Measurements.

2.3.2 Carrier Phase Ambiguity Resolution. There are a multitude of approaches when it comes to resolving the ambiguities in carrier phase measurements [21]. The most common and straightforward method is to use the pseudorange measurement to limit the search area and to model the ambiguity as a constant. This work is not focused around integer ambiguity resolution but rather floating point ambiguity estimation.

2.4 Pseudolite-Based Reference System

2.4.1 Pseudolite Basics. The idea of pseudolites is based on the need to create a reference system similar to GPS for ground-based testing and developing. Since pseudolites are smaller and ground-based they are much more cost efficient then GPS when it comes to hardware development, implementation, and testing. In fact GPS was tested and developed through the use of pseudolites [24]. Pseudolites are a time-of-arrival (TOA) positioning system. Recently, pseudolite packages have decreased in size and increased in capability allowing for a network to be easily setup in a local configuration. The Locata Corporation has developed a pseudolite network capable of achieving navigation accuracy similar to DGPS capabilities. Prior work

has shown this system can achieve a level of accuracy of sub-decimeter positioning error [2] [30]. But pseudolite systems are still subjected to other errors that are associated with ground-based systems, such as multipath fading, vertical geometry, near-far case, nonlinear approximation and measurement errors [30] [10] [11].

Pseudolite systems typically have a higher nonlinearity in the transmitted signals than GPS [10]. This is due to the geometry of the network. The distance away from Earth allows the GPS signals to have less nonlinearity issues than that of a ground-based system that is transmitting on the level of kilometers away. A range measurement can lie anywhere on a circle around the pseudolite. Since the ranges in this case are short compared to GPS, the Taylor series expansion of the measurement is only valid for a small region. This will contribute to filter divergence if the errors grow too large or have extremes dynamics in the system. In GPS the distance is relatively long (20,000 km), thus the region for the linear approximation is larger and allows for convergence in a filter with larger errors. When initializing the position solution with a pseudolite system, it is important to use knowledge of the starting location.

The pseudolite measurements are similar to GPS measurements, except the pseudolite measurements do not contain an error due to the ionosphere. This is due to the fact the pseudolite signals do not travel through the ionosphere since they are ground-based.

2.4.2 Locatalites. Locatalites are a specific type of pseudolite developed by the Locata Corporation. Locata has developed a timing technique referred to as TimeLoc which is used to synchronize their pseudolite networks [5]. This is done by synchronizing the clocks of all transmitters to one pseudolite that is described as the master Locatalite. This results in the following pseudorange measurement

$$\rho = r + T + c\delta t_{rec} + v_\rho + m_\rho \tag{2.17}$$

and carrier phase measurement

$$\phi = \frac{1}{\lambda}(r + c\delta t_{rec} + T + v_\phi + m_\phi) + N \tag{2.18}$$

Since the Locata system has already removed the transmitter clock bias error, there is little value to double differencing the measurements. Instead a single differencing of the pseudolite measurements is performed to remove the receiver clock error. Figure 2.6 shows two signals being transmitted to one receiver. Subtracting the signal of transmitter B from transmitter A results in a single difference measurement with the receiver clock removed. For this example, it is assumed the frequency of the measurement is the same. Locatalites have the capability, however, to transmit on multiple frequencies in the 2GHz ISM band [4].

$$\triangle\rho^{A,B} = \triangle r^{A,B} + \triangle T^{A,B} + \triangle v_\rho^{A,B} + \triangle m_\rho^{A,B} \tag{2.19}$$

and

$$\triangle\phi^{A,B} = \frac{1}{\lambda}(\triangle r^{A,B} + \triangle T^{A,B} + \triangle v_\phi^{AB} + \triangle m_\phi^{A,B}) + \triangle N^{A,B} \tag{2.20}$$

2.4.3 Measurement Errors. As shown above, the pseudolite measurements contain errors similar to GPS measurements. The first major difference between the two is the pseudolite measurements do not travel through the ionosphere, thus troposphere is the only major atmospheric error. Also the Locata system transmitter clocks have been synchronized, removing the transmitter clock bias. The pseudolite pseudorange measurements contain errors from troposphere, multipath, white noise, and receiver clock errors. The carrier phase measurements contain the same errors as the pseudoranges and in addition require an ambiguity in each measurement to be estimated. The receiver clock error can be removed by either using a model and estimating the clock bias or using single difference measurements to remove the receiver clock error.

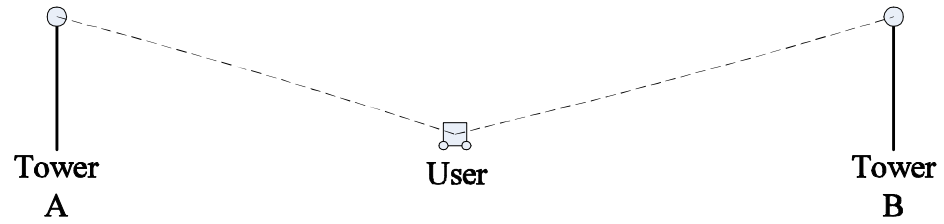

Figure 2.6: Pseudolite Range Example, using Two Signals.

A problem that arises in pseudolite systems due to transmitted signal power is referred to as the near-far problem. The near part of the near-far problem occurs when the strength of one signal is such that it jams the other signals. The far part of the problem occurs when the signal transmitted is too weak to detect when it arrives at the receiver. This occurs in other communication system, it even occurs in a lesser extent with GPS. In GPS the signals are transmitted from similar distances, thus signal power is relatively similar to the signals received. To deal with this issue the Locatalites have been designed to use time division multiple access (TDMA). This sets the duty cycle for when each pseudolite can transmit and avoids jamming other pseudolites.

Another source of error comes from surveying the Locata tower positions. The Locata tower position accuracy is only as good as the survey equipment used. Since the pseudolite system is laid out on the ground, each position is required to be surveyed by the user.

The last source of error, presented in this research, is multipath fading errors. The multipath errors lead to occasional cycle slips in the system. Detection and removal of cycle slips can be difficult at times, depending on the size of the cycle slip and SNR. Cycle slips can occur as small as half a wavelength (6cm), thus they can be difficult to detect. Multipath errors can also be in the form of slow growing errors that ramp up and ramp down over a series of samples.

2.5 Kalman Filter

The Kalman filter is an estimator that is commonly used in navigation filters that contain inertial sensors. This is due to the ability of the Kalman filter to estimate the errors in the inertial measurements. This section includes a brief derivation of the Kalman filter algorithm [20] and leads to the extended Kalman filter [19]. In previous work the inertial sensor has been aided by barometer updates, GPS measurements, LIDAR systems and many other position sensors [26] [12] [20] [9]. The Kalman filter performs well with the fast measurement rate of the inertial data in the mechanization portion of the filter algorithm. Also this type of filter is ideal when updating the inertial-based navigation solution with a system like GPS.

2.5.1 Noise in the Kalman Filter.

There are two applications of noise that occur in the Kalman filter algorithms—process noise ($\mathrm{w}(t_i)$) and measurement noise ($v(t_i)$). Both types are based on zero mean white noise that can be described through a Gaussian probability density function (PDF). Discrete process noise ($\mathrm{w}_d(t_i)$) is described in the Kalman filter algorithm by the covariance matrix, $Q_d(t_i)$

$$E[\mathrm{w}_d(t_i)] = 0 \tag{2.21a}$$

$$E[\mathrm{w}_d(t_i)\mathrm{w}_d^T(t_j)] = \begin{cases} Q_d(t_i) & t_i = t_j \\ 0 & t_i \neq t_j \end{cases} \tag{2.21b}$$

Process noise and measurement noise are assumed to be independent of each other. Measurement noise is also Gaussian white noise and can be described by the following parameters

$$E[v(t_i)] = 0 \tag{2.22a}$$

$$E[v(t_i)v^T(t_j)] = \begin{cases} R(t_i) & t_i = t_j \\ 0 & t_i \neq t_j \end{cases} \tag{2.22b}$$

where $R(t_i)$ is the process noise covariance matrix.

2.5.2 Kalman Filter Algorithm. The Kalman filter is an optimal unbiased estimator [20] [9]. A Kalman filter optimally propagates and updates the state estimates using all knowledge available. Knowledge comes from the covariance of the estimates, process noise, and update noise. Unbiased refers to the idea that the errors associated with the measurements and estimates will be zero mean over time.

A Kalman filter consists of two distinct steps—a propagation step and an update step. The first step involves propagating the estimates using the state model. The state estimates ($x(t)$) are propagated forward in time using the following differential equation

$$\dot{x}(t) = F(t)x(t) + B(t)u(t) + G(t)\mathrm{w}(t) \tag{2.23}$$

where

$$\begin{aligned} F(t) &= \text{process matrix} \\ B(t) &= \text{input matrix} \\ G(t) &= \text{noise matrix} \\ u(t) &= \text{input at time } t \\ \mathrm{w}(t) &= \text{process noise} \end{aligned}$$

The following is a whole state example, used to explain how a Kalman filter is initialized using an initial estimate, x_0, and an initial uncertainty, P_0. The initial state estimates are described in Equation (2.24). In this example the states shown are based on the known starting location (Pos_0), initial velocity (Vel_0), and the initial attitude (Ψ_0).

$$x_0 = \begin{bmatrix} Pos_0 \\ Vel_0 \\ \Psi_0 \end{bmatrix} \tag{2.24}$$

The initial covariance of the state estimates is based on how well the states are known and the process noise. This is even more important when correcting the inertial data and estimating the accelerometer and gyro biases.

$$P_0 = \begin{bmatrix} \sigma_p^2 & 0 & 0 \\ 0 & \sigma_v^2 & 0 \\ 0 & 0 & \sigma_\Psi^2 \end{bmatrix} \tag{2.25}$$

where σ_p^2, σ_v^2,and σ_Ψ^2 are the initial variances that describe the knowledge of the initial position, velocity, and attitude estimates. To implement the model, a difference equation is required for a discrete system. The first step is to compute the transition matrix, Φ_i, given the process matrix, $F(t_i)$, over a small interval ($\triangle t$) using

$$\Phi_i = e^{F(t_i)\triangle t} \tag{2.26}$$

The input matrix, $B(\tau)$ and input $u(\tau)$, are also computed for each epoch using the integral

$$B_d u_d = \int_{t_{i-1}}^{t_i} \Phi(t_i, \tau) B(\tau) u(\tau) d\tau \tag{2.27}$$

Once the difference equation is calculated, the iteration process of the Kalman filter can begin. Figure 2.7 shows how the filter is initialized with an initial estimate and covariance. The equations in Figure 2.7 use a subscript k which refers to the sample at time t_i. The filter propagates the estimate and covariance forward in time until a measurement becomes available. Also shown is how the measurement is incorporated in to the state estimates through the Kalman gain. The Kalman gain provides a weighting factor that is calculated using the current estimate's uncertainty combined with the uncertainty of the update measurement (Equation (2.32)).

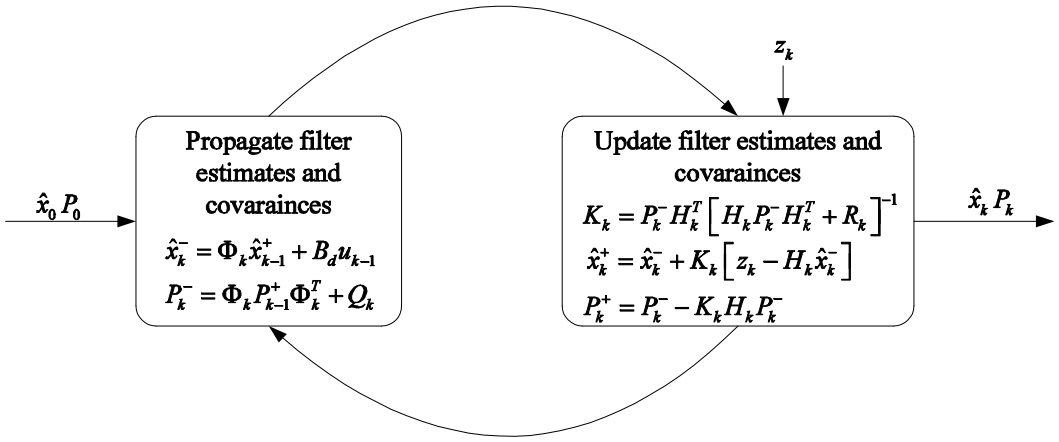

Figure 2.7: The Kalman Filter Algorithm shown as a Looping Process, with the Initial Conditions and Filter Outputs.

In the propagated estimate (Equation (2.28)) there is no term for the process noise included. This is because the expected value of white noise is zero.

$$\hat{x}(t_i^-) = \Phi_i \hat{x}(t_{i-1}^+) + B_d u_d \tag{2.28}$$

The process noise does however increase the uncertainty in the estimate. Thus the discrete noise (Q_d) is contained in the covariance update Equation (2.29). The discrete noise is calculated using the Van Loan technique [9]. The covariance is propagated forward using a combination of the transition matrix and the process noise. The process noise can drive the uncertainty in the estimate to grow rapidly or slowly depending on the dynamics being modeled in the system. For an inertial sensor gyro drift rate, the estimated process noise in a MEMs device will cause the covariance of the estimate to grow rapidly.

$$P(t_i^-) = \Phi_i P(t_{i-1}^+) \Phi_i^T + G_d(t_{i-1}) Q_d(t_{i-1}) G_d^T(t_{i-1}) \tag{2.29}$$

Once the estimate and the covariance have been propagated forward in time, the second step of the Kalman filter updates the state estimates using available mea-

surements. However the update step is only done when measurements are available. The Kalman filter algorithm is written as such that the state estimate and covariance will propagate over time until a measurement becomes available.

The first process in the update step is to calculate the error between the estimate and the measurement (z_i). The estimates ($\hat{x}(t_i^-)$) are transformed into the measurement space using the sensitivity matrix $H(t_i)$. This error is referred to as the residual:

$$r(t_i) = z_i - H(t_i)\hat{x}(t_i^-) \tag{2.30}$$

When applying the measurement update, a weighting factor is calculated. In the Kalman filter, the weighting factor is referred to as the Kalman gain ($K(t_i)$). The Kalman gain is calculated based on the covariance of the measurements and the covariance of the estimates. The covariance of the measurement residuals, Equation (2.31), is calculated as part of the Kalman filter.

$$A(t_i) = H(t_i)P(t_i^-)H^T(t_i) + R(t_i) \tag{2.31}$$

The residual covariance is then used to solve for the Kalman gain:

$$K(t_i) = P(t_i^-)H^T(t_i)[H(t_i)P(t_i^-)H^T(t_i) + R(t_i)]^{-1} \tag{2.32}$$

The Kalman gain is then used to weight the measurement residual. This can be seen in the state estimate update

$$\hat{x}(t_i^+) = \hat{x}(t_i^-) + K(t_i)[z_i - H(t_i)\hat{x}(t_i^-)] \tag{2.33}$$

Also the Kalman gain is used to weight the update of the covariance matrix

$$P(t_i^+) = P(t_i^-) - K(t_i)H(t_i)P(t_i^-) \tag{2.34}$$

There are many different versions of the Kalman filter. The one implemented in this work will be the extended Kalman filter. The extended Kalman filter is based on linearizing the regular Kalman filter using the Taylor series expansion.

2.6 Extended Kalman Filter

The extended Kalman filter is chosen when a system with nonlinearities is included in a navigation filter and the linear Kalman filter can no longer be implemented. The extended Kalman filter is commonly used in GPS systems since GPS measurements are nonlinear. When the extended Kalman filter is used the GPS measurements can be updated into the filter in a linear manner. In the case of GPS, the line-of-site equations are linearized using the first order Taylor series method. The extended Kalman filter is an extension of the linearized Kalman filter. The difference between the linearized and extended Kalman filters is the source of the nominal conditions the algorithm equations are linearized about. For the linearized Kalman filter, the nominal conditions are predetermined by a nominal trajectory that is known prior to implementing the filter. The EKF is based on using the filter estimates as the nominal conditions thus it is dependent on accurately estimating the trajectory.

One would use the linearized filter for a system with a known trajectory that can be precalculated, such as a satellite orbit. On the other hand the linearized Kalman filter will not do so well when it comes to a trajectory that has unmodeled errors and disturbances, such as a plane in flight with wind. The extended Kalman filter would suit this situation better; however, the extended Kalman filter uses the best known position estimate as its linearization condition, thus if this position is not accurate or invalid the filter can diverge. Thus the EKF can be susceptible to measurement observability.

2.6.1 Extended Kalman Filter Equations. This section will present the algorithm for implementing an extended Kalman filter (EKF) [19]. The first step is to derive the propagation equations that will be used in the EKF. The Taylor series expansion is used to linearize the dynamic model and the measurement model.

The process noise in the difference model is expressed as Q_k. This is found using the Van Loan technique [9]. The Van Loan technique calculates the discrete process noise from the linearized state matrix, $F[\hat{x}(t/t_i), t]$, the noise intensity matrix, G, and the continuous process noise covariance, Q. There is no single, precomputed Q_k since this value is also calculated every propagation step along with the transition matrix.

To solve for the propagated state estimate the non-linear differential Equation (2.35) will be evaluated from the time interval of t_{i-1} to t_i (t_i/t_{i-1})

$$\dot{\hat{x}}(t_i/t_{i-1}) = f\left[\hat{x}(t_i/t_{i-1}), u(t), t\right] \tag{2.35}$$

where $f\left[\hat{x}(t_i/t_{i-1}), u(t), t\right]$ is the nonlinear process matrix at time t.

In each propagation step the state dynamic equation is linearized using the nominal conditions. The nominal conditions in an extended Kalman filter are the current state estimates. The first step in linearizing the process matrix is to subtract the nominal state from the true state:

$$[\dot{x}(t) - \dot{x}_n(t)] = f\left[x(t), u(t), t\right] - f\left[\hat{x}(t), u(t), t\right] + G(t)\mathrm{w}(t) \tag{2.36}$$

where

$$\begin{aligned} f[\cdot] &= \text{the nonlinear process matrix} \\ x(t) &= \text{true state at time } t \\ \hat{x}(t) &= \text{estimated state at time } t \end{aligned}$$

The first order Taylor series, Equation (2.36), is linearized about $\hat{x}(t)$ and $u(t)$, resulting in $F(\hat{x}(t), t)$, Equation (2.37).

$$f\left[x(t), u(t), t\right] - f\left[\hat{x}(t), u(t), t\right] \approx \left.\frac{\partial f\left[x(t), u(t), t\right]}{\partial x}\right|_{x=\hat{x}(t), u=\bar{u}(t)} \left[x(t) - \hat{x}(t)\right] \quad (2.37)$$

where $\frac{\partial f[x(t),u(t),t]}{\partial x}$ is the partial derivative of the process matrix with respect to the states (x) at time t.

The perturbation state is defined by $[x(t) - x_n(t)] = \delta x(t)$. The resulting perturbation equation of the states is

$$\dot{\delta x}(t) = \left.\frac{\partial f\left[x(t), u(t), t\right]}{\partial x}\right|_{x=\hat{x}(t), u=\bar{u}(t)} \delta x + G(t)\mathrm{w}(t) \quad (2.38)$$

The propagation equation can be calculated directly in MATLAB using an ODE solver. Using a numerical integrator to find $\hat{x}(t_i^-)$ provides a simpler means of implementing the EKF algorithm. The covariance can then be calculated using a numerical integrator solving the differential Equation (2.39).

$$\dot{P}(t_i/t_{i-1}) = F[\hat{x}(t_i/t_{i-1}), t]P(t_i/t_{i-1}) + P(t_i/t_{i-1})F^T[\hat{x}(t_i/t_{i-1}), t] + G(t_i)Q(t_i)G^T(t_i) \quad (2.39)$$

The nonlinear measurement estimate $(\hat{z}(t_i))$, shown in Equation (2.40), is also linearized using the Taylor series approach.

$$\hat{z}(t_i) = h[\hat{x}(t), t] + v(t) \quad (2.40)$$

where $v(t)$ is the measurement noise.

The nonlinear measurement matrix, $h\left[x(t), t\right]$, is expanded in Equation (2.41).

$$\left[z(t) - \hat{z}(t)\right] = h\left[x(t), t\right] - h\left[\hat{x}(t), t\right] + v(t) \quad (2.41)$$

where

$$\begin{aligned} z(t) &= \text{true measurement} \\ z_n(t) &= \text{estimated measurement} \\ h\left[\hat{x}(t), t\right] &= \text{nonlinear measurement matrix based on the estimated state} \\ h\left[x(t), t\right] &= \text{nonlinear measurement matrix based on the true state} \end{aligned}$$

Then taking the partial derivatives in terms of the states and evaluating about the nominal conditions, $\hat{x}(t)$, results in

$$h\left[x(t), t\right] - h\left[\hat{x}(t), t\right] \approx \left.\frac{\partial h\left[\hat{x}(t), t\right]}{\partial x}\right|_{x=\hat{x}(t)} \delta x(t) \tag{2.42}$$

where $\frac{\partial h[\hat{x}(t),t]}{\partial x}$ is the partial derivative of the measurement matrix with respect to x at time t.

The resulting measurement equation in terms of the perturbations, $\delta x(t)$, is shown in Equation (2.43).

$$\delta z(t) = \left.\frac{\partial h\left[\hat{x}(t), t\right]}{\partial x}\right|_{x=\hat{x}(t)} \delta x(t) + v(t) \tag{2.43}$$

The remainder of this section presents the algorithm used to implement the extended Kalman filter [19]. The nominal condition is based on the propagated estimate from Equation (2.35). When there are no measurements available to incorporate into the filter estimates, then the state estimates are passed on in the update step as

$$\hat{x}(t_i^+) = \hat{x}(t_i^-) \tag{2.44}$$

and the covariance

$$P(t_i^+) = P(t_i^-) \tag{2.45}$$

When the measurements are available Equations (2.46) to (2.51) are used to update the state estimates and covariance with the current measurements. The first step in the update process is to calculate the Kalman gain, $K(t_i)$,

$$K(t_i) = P(t_{i+1}^-)H^T[\hat{x}(t_i^-), t_i]\left[H[\hat{x}(t_i^-), t_i]P(t_i^-)H^T[\hat{x}(t_i^-), t_i] + R(t_i)\right]^{-1} \tag{2.46}$$

where

$$H[\hat{x}(t_i^-), t_i] = \left.\frac{\partial h\left[\hat{x}(t), t\right]}{\partial x}\right|_{x=\hat{x}(t_i^-)}$$

The extended Kalman filter is developed on the idea of incorporating perturbations into the previous state estimates. In an attempt to develop an equation to calculate the whole state a few steps are needed. The first step is to calculate the error state propagation equation, also referred to as the perturbation equation. To calculate this equation a first order Taylor series is used.

When updating the extended Kalman filter, the error state estimates are calculated using the Kalman gain and incorporating the new measurement

$$\widehat{\delta x}\left(t_i^+\right) = \widehat{\delta x}\left(t_i^-\right) + K(t_i)\left[(z_i - \hat{z}(t_i/t_{i-1})) - H(\hat{x}(t_i^-), t_i)\widehat{\delta x}\left(t_i^-\right)\right] \tag{2.47}$$

where $\widehat{\delta x}$ is the estimated error state.

The error of the state estimate is zero after it has been incorporated in the update step. This then means the error after propagating is also zero

$$\widehat{\delta x}\left(t_i^-\right) = 0 \tag{2.48}$$

Therefore the resulting measurement update for the error state becomes

$$\widehat{\delta x}\left(t_i^+\right) = K(t_i)\left[(z_i - \hat{z}(t_i/t_{i-1}))\right] \tag{2.49}$$

Equation (2.49) is exactly the residual of the whole state estimate—therefore the whole state estimate can be expressed as Equation (2.50). This is true since the whole state is the propagated estimate plus the correction term in Equation (2.49).

$$\hat{x}(t_i^+) = \hat{x}(t_i^-) + K(t_i)\left(z_i - h[\hat{x}(t_i^-), t_i]\right) \tag{2.50}$$

The residual is calculated from the nonlinear function $h[\hat{x}(t_i^-), t_i]$. The resulting $h[\hat{x}(t_i^-), t_i]$ is then subtracted from the current measurement, z_i.

The covariance update is based on the same equation used in the standard Kalman filter.

$$P(t_i^+) = P(t_i^-) - K(t_i)H[\hat{x}(t_i^-), t]P(t_i^-) \tag{2.51}$$

This section explained how the extended Kalman filter algorithm is implemented using nonlinear process and measurement models. The next section will discuss how failure detection can be implemented in the extended Kalman filter algorithm.

2.7 Failure Detection

The idea of failure detection is to find and remove measurements that contain errors. Cycle slips are errors that commonly occur in GPS and pseudolite-based systems. Having the ability to reject errors increases the reliability of a system. Failure detection can be done many different ways. A basic approach to failure detection is to use a residual monitoring technique [20]. It is common practice to use the residual in a Kalman filter to detect and reject bad measurements. The residual and residual covariance are calculated at each update in the Kalman filter algorithm. Using the residual (Equation (2.30)) for detecting failures is possible since the residual is a zero mean Gaussian distributed variable with a specified variance (Equation (2.31)). A failure is declared when the threshold, in terms of standard deviations, is exceeded. Thus, when a residual is some specified number of standard deviations away from the expected value then a failure is declared. This type of

algorithm performs well when dealing with cycle slips and slow growing errors that are large enough to cause the residual to exceed the threshold. This implementation was used in [25], where the residual (r_{k_i}) is divided by the residual standard deviation ($\sigma_{r_{k_i}}$) the resulting ratio is the same test statistic mentioned above. The number of sigma the residual is from the standard deviation (t_{k_i}) is calculated as

$$t_{k_i} = \frac{r_{k_i}}{\sigma_{r_{k_i}}} \tag{2.52}$$

Another failure detection method discussed in [20] used statistical hypothesis testing for the likelihood function. This method uses a moving window that incorporates the statistics of the past N residuals and residual variances. It then uses the sequence to determine if a failure occurred inside the window. The size of the window is normally between 5 and 20 samples. This function is describe by

$$L_{N_k}(t_i) = c_k(t_i) - \frac{1}{2}\sum_{j=i-N+1}^{i} \frac{r_k^2(t_j)}{\sigma_k^2(t_j)} \tag{2.53}$$

where $c_k(t_i)$ does not contain information about the likelihood of a failure [20].

This type of likelihood function is good at detecting failures that occur randomly over time but that may not violate the residual threshold technique previously discussed. However this technique results in a delay in detecting a bad measurement. The length of the delay will depend on the size of the error, the threshold, and the noise of the previous measurements.

A third failure detection technique is to use a multiple filter approach. In this case a failure detection algorithm using the residual monitoring technique can trigger a second filter to be spawned, hypothesizing the existence of a cycle slip. Both filters would then exist until one or the other was determined valid by hypotheses testing.

This technique can become cumbersome with processing and implementation if there are many failures in a short time period. For N failures there will be 2^N

filters. To reduce the level of computation then the size of N would be restricted. When implementing a restriction of the number of filters then it is possible more failures would be declared. This would work by resetting the ambiguity and trimming the non-failure filter. This would then make room for a new failure to be declared. Declaring a false alarm on one measurement will change the confidence in that measurement over a short period of time. This is less likely to impact the filter then incorporating a measurement with the wrong ambiguity.

2.8 Summary

This section presented many topics in navigation that are used when implementing an inertial and pseudolite-based navigation system. The topics discussed consisted of inertial, measurement mechanization, the global positioning system, pseudolite technology, Kalman filtering, and failure detection. The extended Kalman filter was presented for use with a nonlinear navigation system, such as the pseudolite system. The integration of the pseudolite and inertial system will be shown in the next chapter. This will include how the failure detection is implemented in the extended Kalman filter algorithm.

III. Design of the Pseudolite and Inertial Navigation Filter

This chapter focuses on the pseudolite and INS integration, along with incorporating failure detection. The integration was done through the use of an extended Kalman filter. The development of the filter includes the dynamic system model, the measurement model, and the floating point carrier phase ambiguity estimation used in this work. The dynamic model section will discuss the inertial error model and the noise sources. The following section discusses the nonlinear measurement model. The measurement model is created using the pseudoranges and single differenced carrier phase measurements from the pseudolite system. The failure detection algorithm implementation will then be explained. The failure detection algorithm was implemented with the navigation filter to reduce errors and increase reliability the phase measurements. The navigation filter, with failure detection, was tested using real data. This includes conducting a field experiment and developing simulation data from the field work.

3.1 Navigation Filter

The navigation filter implemented in this research was derived from the extend Kalman filter algorithm presented in Chapter 2. This filter uses an error state approach to make corrections to the inertial mechanization solution. Also the navigation solution is fed back to the INS mechanization algorithm to keep the errors small in the navigation filter. The inertial sensor was tightly integrated with the pseudolite measurements. The pseudolite measurements are capable of up to a ten Hertz update rate, depending on the output choice. The pseudolite system can operate at 10Hz in binary output mode or a max rate of 2Hz in ASCII output mode. Most of the work presented here used the 2Hz data rate. Two Hertz was used since the growth of errors in the inertial mechanization is relatively small over this period.

3.1.1 Dynamic System Model. The dynamics in the navigation system are comprised of an error model of the inertial system, a clock model for the pseudoranges, and process noise for the ambiguity estimates. A local level error model was used when implementing the inertial system dynamics. The dynamics used are based on the ones developed and described in [33].

The error states in the navigation system due to the inertial error model are shown in detail to their corresponding variable

$$
\begin{aligned}
x_1 &= \delta P_N && \text{Position error in the North direction (meters)} \\
x_2 &= \delta P_E && \text{Position error in the East direction (meters)} \\
x_3 &= \delta P_D && \text{Position error in the Down direction (meters)} \\
x_4 &= \delta v_N && \text{Velocity error in the North axis (meters/second)} \\
x_5 &= \delta v_E && \text{Velocity error in the East axis (meters/second)} \\
x_6 &= \delta v_D && \text{Velocity error in the Down axis (meters/second)} \\
x_7 &= \delta \psi_N && \text{Angle error about the North axis (radians)} \\
x_8 &= \delta \psi_E && \text{Angle error about the East axis (radians)} \\
x_9 &= \delta \psi_D && \text{Angle error about the Down axis (radians)} \\
x_{10} &= a_{bias_x} && \text{Bias in the x-axis accelerometer (meters/second}^2\text{)} \\
x_{11} &= a_{bias_y} && \text{Bias in the y-axis accelerometer (meters/second}^2\text{)} \\
x_{12} &= a_{bias_z} && \text{Bias in the z-axis accelerometer (meters/second}^2\text{)} \\
x_{13} &= \omega_{bias_x} && \text{Bias in the x-axis gyroscope (radians/second)} \\
x_{14} &= \omega_{bias_y} && \text{Bias in the y-axis gyroscope (radians/second)} \\
x_{15} &= \omega_{bias_z} && \text{Bias in the z-axis gyroscope (radians/second)}
\end{aligned}
$$

The inertial error model used in this research was developed by [33], where the INS error model is derived in detail. This inertial error model provides a linear dynamic

matrix as shown in Equation (3.1).

$$F_{ins} = \begin{bmatrix} 0_{3x3} & I_{3x3} & 0_{3x3} & 0_{3x3} & 0_{3x3} \\ C_e^n G C_n^e & -2C_e^n \Omega_{ie}^e C_n^e & f^n \times & C_b^n & 0_{3x3} \\ 0_{3x3} & 0_{3x3} & -(C_e^n \omega_{ie}^e) \times & 0_{3x3} & -C_b^n \\ 0_{3x3} & 0_{3x3} & 0_{3x3} & -\frac{1}{T_a} I_{3x3} & 0_{3x3} \\ 0_{3x3} & 0_{3x3} & 0_{3x3} & 0_{3x3} & -\frac{1}{T_\omega} I_{3x3} \end{bmatrix} \tag{3.1}$$

where

$$\begin{aligned} C_e^n &= \text{Earth to navigation frame rotation matrix} \\ C_n^e &= \text{navigation to Earth frame rotation matrix} \\ f^n &= \text{force in the navigation frame} \\ G &= \text{noise intensity matrix} \\ \Omega_{ie}^e &= \text{Earth rate} \\ T_a &= \text{time constant for accelerometer bias} \\ T_\omega &= \text{time constant for gyroscope bias} \\ C_b^n &= \text{body to navigation frame rotation matrix} \end{aligned}$$

The bias estimation model for the accelerometers and gyroscopes is driven by white noise. This model was shown in Equation (2.5) where the accelerometer bias noise is noted as $w_{bias}^a$and the gyroscope bias noise as w_{bias}^ω. There is also inertial sensor measurement noise w_{ins}^f and w_{ins}^ω, shown in Equation (2.3) and Equation (2.4). Therefore there are 12 white noise sources associated with the inertial model. This

leads to the inertial noise intensity matrix G_{ins}.

$$G_{ins} = \begin{bmatrix} 0_{3x3} & 0_{3x3} & 0_{3x3} & 0_{3x3} \\ C_b^n & 0_{3x3} & 0_{3x3} & 0_{3x3} \\ 0_{3x3} & -C_b^n & 0_{3x3} & 0_{3x3} \\ 0_{3x3} & 0_{3x3} & I_{3x3} & 0_{3x3} \\ 0_{3x3} & 0_{3x3} & 0_{3x3} & I_{3x3} \end{bmatrix} \tag{3.2}$$

3.1.2 Pseudolite Inertial Integration. The navigation filter was designed around an inertial navigation system that was tightly integrated with raw pseudolite measurements. The navigation filter process model, in its entirety, is shown in Figure 3.1. Tight integration was used for several reasons. First, tight integration gives insight into the raw phase measurements, aiding in the ability to implement failure detection. If the system was integrated using loose coupling, failure detection would not be as efficient. Since the failure detection is done in conjunction with positioning, bad measurements can be detected and removed before being incorporated in a position solution. Also it keeps from having to design a separate Kalman filter for the pseudolite measurements. Ultra-tight integration was not an option for this work. Ultra-tight integration could help in the detection and removal of multipath errors. For this work only the pseudolite raw measurements were available. Since the inertial system is tightly integrated with the pseudolite measurements the measurement model is based on

$$\delta\hat{z}(t) = z_{pl}(t) - \hat{z}(t) \tag{3.3}$$

where $z_{pl}(t)$ is the pseudolite measurement and $\hat{z}(t)$ is the estimated pseudolite measurement.

Integration of the pseudolite system will also require augmentation to the states described earlier. The carrier phase measurements contain floating point ambiguities

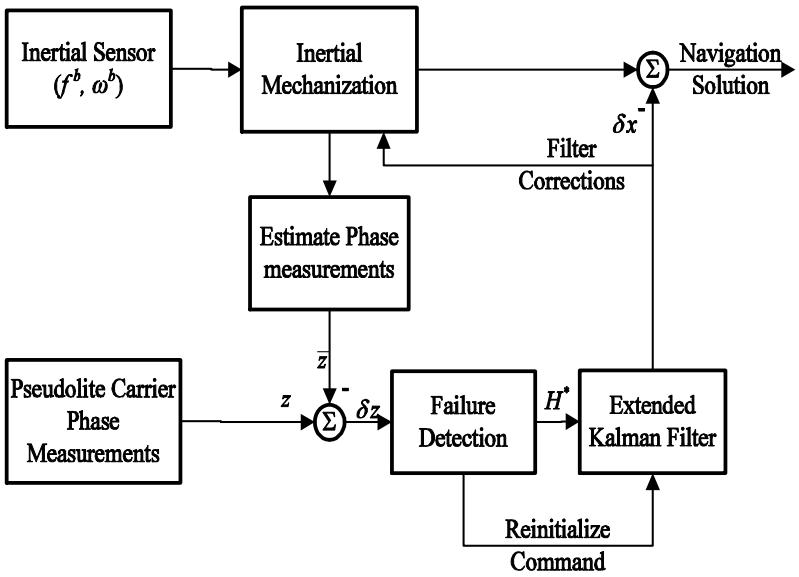

Figure 3.1: The Navigation Filter Model, showing the Pseudolite Measurements Tightly Integrated with the INS.

that will be estimated as part of the navigation filter algorithm. The number of ambiguities depends on the number of available measurements at each epoch during the navigation period. For this research a maximum of 20 carrier phase measurements were available. This results in 19 single difference measurements using one signal as the reference for all observations. A number 1 through 20 is used to identify the pseudorandom noise (PRN) frequency of each pseudolite in the system. For example, if PRN 1 is the reference then the single differenced ambiguity for PRN k will be $\triangle N^{1,k}$ where k is any number from 2 to 20.

In addition to the ambiguity states there will also be another two states used to estimate the clock bias and drift in the pseudorange measurements. The clock model [9] Equation (3.4) is comprised of two states, a bias x_{clk_1} and a drift x_{clk2}. Each state is driven by zero mean white Gaussian noise, w_{clk1} and w_{clk_2}. The bias, x_{clk_1}, is used to estimate the pseudorange error due to the receiver clock bias in the pseudolite measurements. This is a similar model to the one used when estimating

the receiver clock bias in GPS pseudoranges.

$$\begin{bmatrix} \dot{x}_{clk_1} \\ \dot{x}_{clk_2} \end{bmatrix} = \begin{bmatrix} 0 & 1 \\ 0 & 0 \end{bmatrix} \begin{bmatrix} x_{clk_1} \\ x_{clk_2} \end{bmatrix} + \begin{bmatrix} \mathrm{w}_{clk_1} \\ \mathrm{w}_{clk_2} \end{bmatrix} \tag{3.4}$$

The pseudolite system requires up to an additional 21 states in the navigation filter. They include the 2 states for the clock model and 19 states to estimate the single differenced ambiguities. The inertial sensor requires the 15 states described above. The navigation filter then consists of 36 states total. The augmented state vector for the navigation filter is shown in Equation (3.5). The variables δP^n, δv^n, ψ^n, a^n_{bias} and, ω^n_{bias} are all $3x1$ vectors.

$$\delta x = \begin{bmatrix} \delta P^n \\ \delta v^n \\ \delta \psi^n \\ a^n_{bias} \\ \omega^n_{bias} \\ x_{clk_1} \\ x_{clk_2} \\ \triangle N^{1,2} \\ \vdots \\ \triangle N^{1,k} \end{bmatrix} \tag{3.5}$$

The process matrix F is also augmented to include the dynamics of the pseudolite measurements. The pseudolite receiver clock states and the floating point ambiguity states do not impact the dynamics of the inertial model directly, since the systems are independent. The clock dynamic matrix (F_{clk}) is shown in Equation

(3.4). The ambiguity dynamic matrix (F_N) is nxn and equal to zero, $F_N = 0_{nxn}$.

$$F = \begin{bmatrix} F_{ins} & 0_{15x2} & 0_{15xn} \\ 0_{2x15} & Fclk & 0_{2xn} \\ 0_{nx15} & 0_{nx2} & F_N \end{bmatrix} \tag{3.6}$$

The noise intensity matrix (G) is augmented to apply a small amount of process noise to the ambiguity states. This step is done to keep the floating point solution from converging to a constant. Additive white noise is applied to each single differenced ambiguity. The white noise is independent for each single difference observation, $\mathrm{w}_N^{1,k}$

$$\begin{aligned} E[w_N^{1,k}(t)] &= 0 \\ E[w_N^{1,k}(t) w_N^{1,k}(t+\tau)] &= 1x10^{-4} \end{aligned}$$

The inertial noise intensity matrix (G_{ins}) was defined in Equation (3.2), while G_{clk} and G_N are identity matrices corresponding to the noise sources included in the clock model ($G_{clk} = I_{2x2}$) and ambiguity states ($G_N = I_{nxn}$).

$$G = \begin{bmatrix} G_{ins} & 0_{15x2} & 0_{15xn} \\ 0_{2x12} & G_{clk} & 0_{2xn} \\ 0_{nx12} & 0_{nx2} & G_N \end{bmatrix} \tag{3.7}$$

3.1.3 Measurement Model. The measurement model was derived using pseudoranges and single difference carrier phase measurements. The pseudolite measurement model is nonlinear but is linearized using a first order Taylor series, as part of the extended Kalman filter algorithm.

$$\hat{z}(t) = H[\hat{x}(t_i^-), t_i] \tag{3.8}$$

The measurement model is linearized at each epoch using a first order Taylor series approximation. The error due to the troposphere was removed from the pseudorange and carrier phase measurements using a model based on the trajectory and atmospheric conditions [30]. The pseudorange and phase measurements are estimated using Equations (3.9) and (3.10). The pseudorange estimate ($\hat{\rho}_n$) is based on the location (x_n, y_n, and z_n) of the tower n and the current receiver position. The current receiver position is calculated using the best estimate from the propagation algorithm ($\hat{x}_u$, $\hat{y}_u$, and $\hat{z}_u$). The clock error, $c\delta t$, is estimated inside the navigation filter using the clock model described above, Equation 3.4.

$$\hat{\rho}_n = \sqrt{(x_n - \hat{x}_u)^2 + (y_n - \hat{y}_u)^2 + (z_n - \hat{z}_u)^2} + \widehat{c\delta t} \tag{3.9}$$

The carrier phase estimate ($\hat{\phi}_n$) is modeled using the same range calculation as the pseudorange estimate but in this case the clock is not removed by the clock model. Also the ambiguity, N_n, would also need to be estimated in terms of cycles. Each carrier phase measurement may not have the same wavelength, since two different carrier frequencies are in use in this pseudolite system. Thus the wavelengths, λ_n, correspond to the n^{th} carrier phase measurement.

$$\hat{\phi}_n = \frac{1}{\lambda_n}\sqrt{(x_n - \hat{x}_u)^2 + (y_n - \hat{y}_u)^2 + (z_n - \hat{z}_u)^2} + \hat{N}_n + \widehat{c\delta t} \tag{3.10}$$

The next step will include forming the single difference phase estimates based on Equation (3.10). For the derivation of the measurement model, PRN 1 was used as the master for all single difference measurements. The notation $1, n$ refers to PRN 1 minus PRN n.

The phase measurements used in this work are converted to meters. This is done by multiplying each real phase measurement by its corresponding wavelength (λ_n). Thus the single difference phase estimate is also estimated in meters. The resulting single difference phase estimate ($\lambda\Delta\hat{\phi}^{1,n}$) consists of the differenced ranges

between PRN 1 and n and the ambiguity ($\Delta N^{1,n}$) estimated by the filter:

$$\begin{aligned} \lambda\Delta\hat{\phi}^{1,n} &= \sqrt{(x_1-\hat{x}_u)^2+(y_1-\hat{y}_u)^2+(z_1-\hat{z}_u)^2} - \\ &\quad \sqrt{(x_n-\hat{x}_u)^2+(y_n-\hat{y}_u)^2+(z_n-\hat{z}_u)^2} + \Delta\hat{N}^{1,n} \end{aligned} \tag{3.11}$$

Since the phase measurements are multiplied by their corresponding wavelength, the single difference ambiguity ($\Delta N^{1,n}$) will also be in meters. Converting the phase measurements to meters is done since there is only one master phase measurement used as the reference for all the signals. The measurement matrix ($h[\hat{x}(t_i^-), t_i]$) is formulated using the pseudorange and single difference phase estimates, resulting in the following model

$$h[\hat{x}(t_i^-), t_i] = \begin{bmatrix} \sqrt{(x_1-\hat{x}_u)^2+(y_1-\hat{y}_u)^2+(z_1-\hat{z}_u)^2} + \widehat{c\delta t} \\ \vdots \\ \sqrt{(x_n-\hat{x}_u)^2+(y_n-\hat{y}_u)^2+(z_n-\hat{z}_u)^2} + \widehat{c\delta t} \\ \Delta\hat{r}^{1,2} + \Delta\hat{N}^{1,2} \\ \vdots \\ \Delta\hat{r}^{1,n} + \Delta\hat{N}^{1,n} \end{bmatrix} \tag{3.12}$$

where the range notation is defined as

$$\Delta\hat{r}^{1,n} = \hat{r}_1 - \hat{r}_n \tag{3.13}$$

$$\hat{r}_1 = \sqrt{(x_1-\hat{x}_u)^2+(y_1-\hat{y}_u)^2+(z_1-\hat{z}_u)^2} \tag{3.14}$$

$$\hat{r}_n = \sqrt{(x_n-\hat{x}_u)^2+(y_n-\hat{y}_u)^2+(z_n-\hat{z}_u)^2} \tag{3.15}$$

The sensitivity matrix, $h[\hat{x}(t_i^-), t_i]$, is then linearized by taking the partial derivatives in terms of each state and then evaluating the result using the current filter estimates.

The resulting linearized matrix, $H(t)$, is shown in Equation (3.16).

$$\left.\frac{\partial h[\hat{x}(t_i^-), t_i]}{\partial x}\right|_{x=x_n} = \begin{bmatrix} \frac{(x_1-x_u)}{\hat{r}_1} & \frac{(y_1-y_u)}{\hat{r}_1} & \frac{(z_1-z_u)}{\hat{r}_1} & 0 & \cdots & 0 & -1 & 0 & 0 & 0 & \cdots & 0 \\ \vdots & \vdots & \vdots & \vdots & \ddots & \vdots & \vdots & 0 & \vdots & \vdots & \ddots & \vdots \\ \frac{(x_n-x_u)}{\hat{r}_n} & \frac{(y_n-y_u)}{\hat{r}_n} & \frac{(z_n-z_u)}{\hat{r}_n} & 0 & \cdots & 0 & -1 & 0 & 0 & 0 & \cdots & 0 \\ A_x^{1,2} & A_y^{1,2} & A_z^{1,2} & 0 & \cdots & 0 & 0 & 0 & 1 & 0 & \cdots & 0 \\ A_x^{1,3} & A_y^{1,3} & A_z^{1,3} & 0 & \cdots & 0 & 0 & 0 & 0 & 1 & \cdots & 0 \\ \vdots & \vdots & \vdots & \vdots & \ddots & \vdots & \vdots & 0 & \vdots & \vdots & \ddots & \vdots \\ A_x^{1,n} & A_y^{1,n} & A_z^{1,n} & 0 & \cdots & 0 & 0 & 0 & 0 & 0 & \cdots & 1 \end{bmatrix} \tag{3.16}$$

where $\hat{r}_n$ is the estimated range defined in Equation (3.15). The linearized single difference measurement notation, that corresponds with Equation (3.16), is as follows

$$A_x^{1,n} = \frac{(x_1 - x_u)}{\hat{r}_1} - \frac{(x_n - x_u)}{\hat{r}_n} \tag{3.17}$$

$$A_y^{1,n} = \frac{(y_1 - y_u)}{\hat{r}_1} - \frac{(y_n - y_u)}{\hat{r}_n} \tag{3.18}$$

$$A_z^{1,n} = \frac{(z_1 - z_u)}{\hat{r}_1} - \frac{(z_n - z_u)}{\hat{r}_n} \tag{3.19}$$

The resulting measurement matrix is in terms of the error states that make up the navigation filter.

3.1.4 Floating Point Ambiguity Estimation. The ambiguities in the pseudolite phase measurements are not integers, such as the case in GPS phase measurements. In the case of pseudolite phase measurements the ambiguities are estimated using a floating point solution. The procedure for estimating the ambiguities begins with an initial estimate. This estimate relies on using the pseudorange. The single difference pseudorange measurements are subtracted from the single difference phase measurements.

$$\triangle \hat{N}_0^{1,n} = \lambda_1 \phi_1 - \lambda_n \phi_n - \triangle \rho^{1,n} \tag{3.20}$$

where $\triangle\rho^{1,n}$ is the single difference pseudorange measurements.

The resulting value is the initial estimate of the ambiguity ($\triangle\hat{N}_0^{1,n}$). However, there is still multipath and noise errors included in this estimate. Since the pseudorange is used then the uncertainty of the ambiguity is set exactly to the covariance of the pseudorange (σ_ρ^2). The initial covariance matrix of the ambiguities is

$$P_{N_0} = \begin{bmatrix} \sigma_\rho^2 & 0 & \cdots & 0 & 0 \\ 0 & \sigma_\rho^2 & \cdots & 0 & 0 \\ \vdots & \vdots & \ddots & \vdots & \vdots \\ 0 & 0 & \cdots & \sigma_\rho^2 & 0 \\ 0 & 0 & \cdots & 0 & \sigma_\rho^2 \end{bmatrix} \tag{3.21}$$

The Kalman filter will then be used to correct the ambiguity at each measurement update. Over time the ambiguity estimates will converge to an accurate set of ambiguities that agree with the set of measurements at each iteration. When a cycle slip is detected, the ambiguity that contains the error is re-initialized using the pseudorange measurements using Equation (3.20). The intention here is to keep the filter from diverging. If the ambiguity was reset with a bad estimate, then the filter could diverge. To avoid this, the ambiguities are always reset using the pseudorange. The covariance is also reset when an ambiguity is re-initialized. To reset the covariance only the row and column of the ambiguity in question are changed. Shown below, in Equation (3.22), is how the covariance for the second ambiguity estimate is reset.

$$P_{N_R} = \begin{bmatrix} & 0 & & & \\ 0 & \sigma_\rho^2 & \cdots & 0 & 0 \\ & \vdots & & & \\ & 0 & & & \\ & 0 & & & \end{bmatrix} \tag{3.22}$$

The noise error variance in the pseudorange measurements (σ_ρ^2) is 2.5 meters. The noise error variance in the carrier phase measurements (σ_ϕ^2) is 1cm.

3.2 Failure Detection Algorithm

In this research there were two different implementations of a failure detection algorithm. The first one is based on residual monitoring [20]. The other is based observing the residuals over time in a moving window [20].

3.2.1 Residual Threshold Method. A failure detection algorithm was designed using the idea of residual monitoring inside the Kalman filter. This algorithm compares the residual of each individual measurement with its corresponding standard deviation to detect a failure. The failure detection is accomplished after the system is propagated and right before the measurement is incorporated (see Figure 3.2). The navigation flow chart, shown in Figure 3.2, also describes how the filter is implemented step by step. This is important since the failure detection will then identify and remove the measurements that contain errors keeping them from corrupting the navigation solution at the update step.The idea of using the residual to detect a failure was decided upon after researching other methods such as Equation (2.53) [20], Equation (2.52) [26], and SNR-based [1] approaches. The SNR-based approach refers to the use of the SNR measurement to determine when a cycle slip occurs [1] [30]. A threshold was set so that when it was exceeded the cycle slip was declared. The only problem with the SNR method is that, when the SNR is high there is no guarantee a cycle slip does not occur in the phase measurements.

The residual monitoring approach was chosen for the ability to incorporate this algorithm in the navigation filter using information that was readily available. Also since the cycle slips that are to be detected occur fairly quickly, most often within one sample, a single error detection can be sufficient to removing the majority of errors. If a false alarm is detected with this method, then the ambiguity is re-initialized as

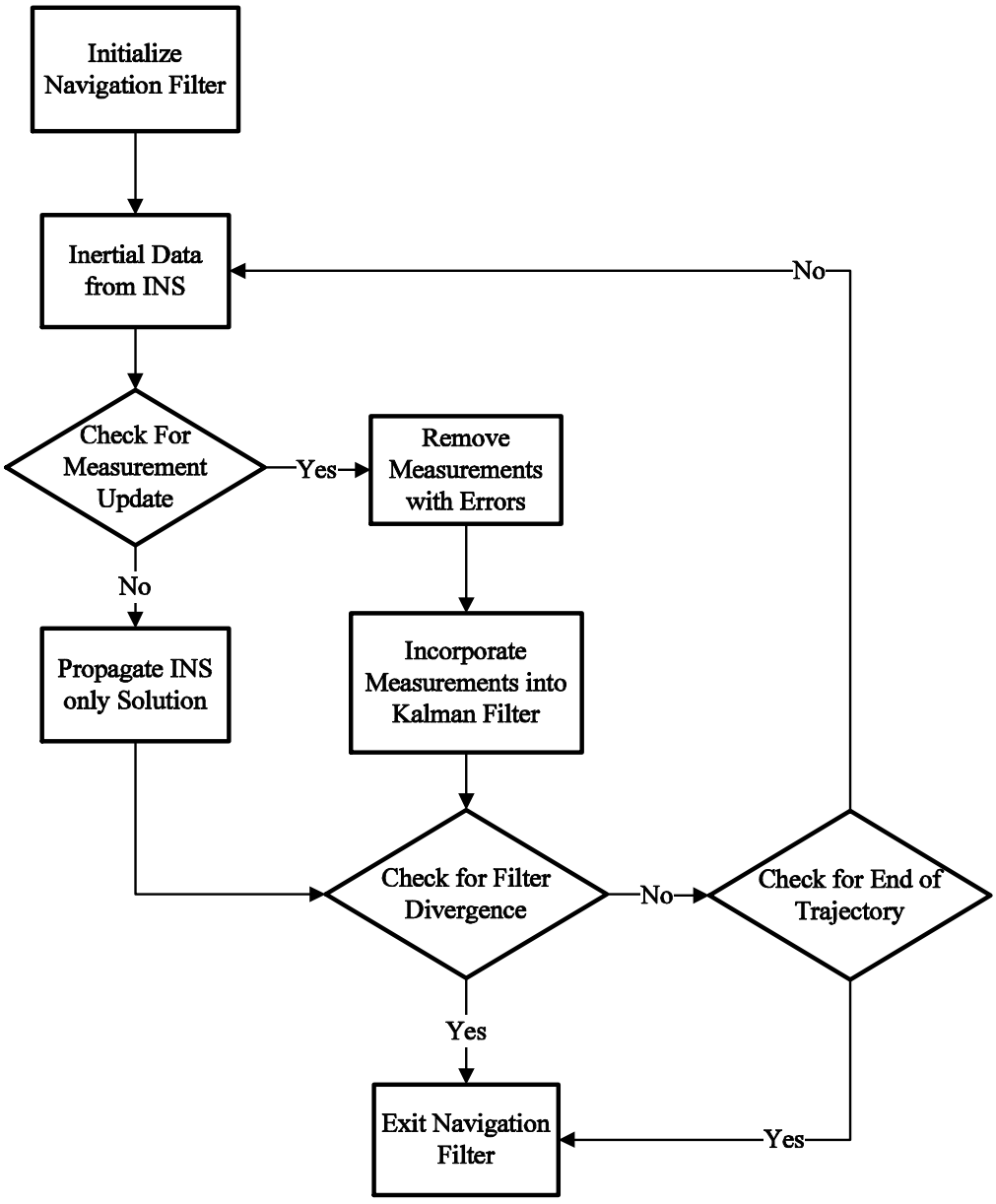

Figure 3.2: The Kalman Filter Decision Process Model with Failure Detection.

described above. The ambiguity states would then converge to accurate estimates over a few iterations.

The threshold for detection was set to 3σ as a starting point to analyze the performance of the algorithm. The threshold was varied to observe the sensitivity of detecting errors while also trying to avoid false alarms. The ability to detect errors will depend on the quality of the inertial sensor. This can be seen in Equation (2.31), where the residual covariance is dependent on the value of the estimated process noise. Larger estimated process noise will result in larger residual standard deviations. This will increase the threshold on the residual making small errors in the phase measurement more difficult to detect.

3.2.2 Moving Window Method. This method uses a moving window over a set number of samples to calculate the likelihood of a failure. The algorithm used 10 samples, in this research, due to the type of errors being modeled. The errors in the phase measurements either happen instantaneously or over a slow growing rate. There are a few steps and conditions required to properly implement Equation (2.53). The moving window assumes the first N samples are error free. If the initial N samples are not error free the algorithm will reject the measurement and re-initialize the window. The window is always re-initialized after any failure detection. The moving window method requires N-1 samples from the current epoch to be stored and used in the next epoch. To declare a failure using the moving window a threshold is required. One note about setting the threshold is the likelihood values of this method becomes more negative as the failures grow larger and more often.

3.3 Field Experiment

A road test was conducted on an inactive runway at area B of Wright-Patterson AFB. The field test consisted of setting up a Locata pseudolite network and conducting a data collection with a navigation reference system. The equipment and support

for this experiment was provided by the Advanced Navigation Technology (ANT) Center at the Air Force Institute of Technology (AFIT). The navigation reference system consisted of a pseudolite receiver, two GPS receivers, and two inertial sensors. The GPS receivers were NovAtel OEM IVs. For the inertial sensors a Microbotics MIDG MEMs sensor was used, while the other was the Honeywell HG1700 IMU, integrated with the NovAtel Black Diamond System (BDS). The navigation sensors were installed on the ANT Center's golf cart (also referred to as the RAVEN). The entire configuration is shown in Figure 3.3.

A pseudolite tower consisted of a survey antenna, a pseudolite receive antenna, and two pseudolite transmit antennas, as shown in Figure 3.4. The survey antenna was installed to be in-line with the phase centers of the pseudolite antennas. The pseudolites used patch antennas as the transmitters and receivers.

Surveying the pseudolite network consisted of recording stationary GPS data over a 15 minute period. The GPS data of each tower was then combined with local reference stations to resolve a position estimate with an expected accuracy of better than 1cm. There are some other errors that need to be considered in the Locata tower position accuracy. Wind can move the tower approximately $1 - 2$cm in any direction, and also the towers can settle in the ground over time attributing another 5 to 10cm of error. The location of pseudolite tower positions and the origin of the receiver are shown in Table 3.1.

The pseudolite tower positions 1 through 6 are depicted in Figure 3.5 relative to the runway, outlined in the figure, which was used during the experiment. Also the origin of the vehicle trajectory is highlighted and marked with O. The geometry of the system was ideal in the horizontal axes. Unfortunately, there was not much of a vertical difference between the six towers, thus the vertical geometry was not adequate. The expected errors in horizontal position are around 10cm, while the error in the vertical channel is expected to be on the order of 10 meters. Using

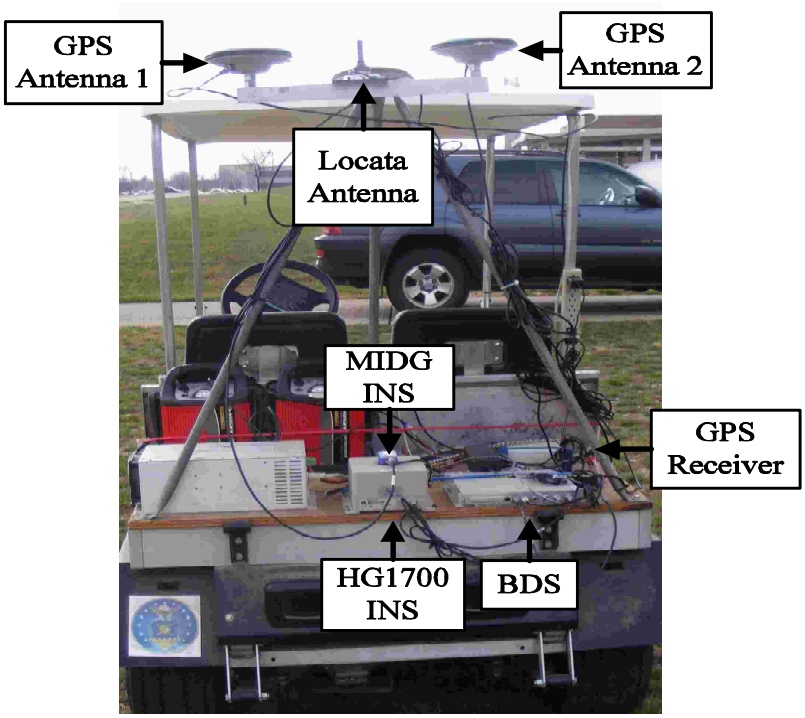

Figure 3.3: Navigation Sensor Installation on the ANT Center RAVEN.

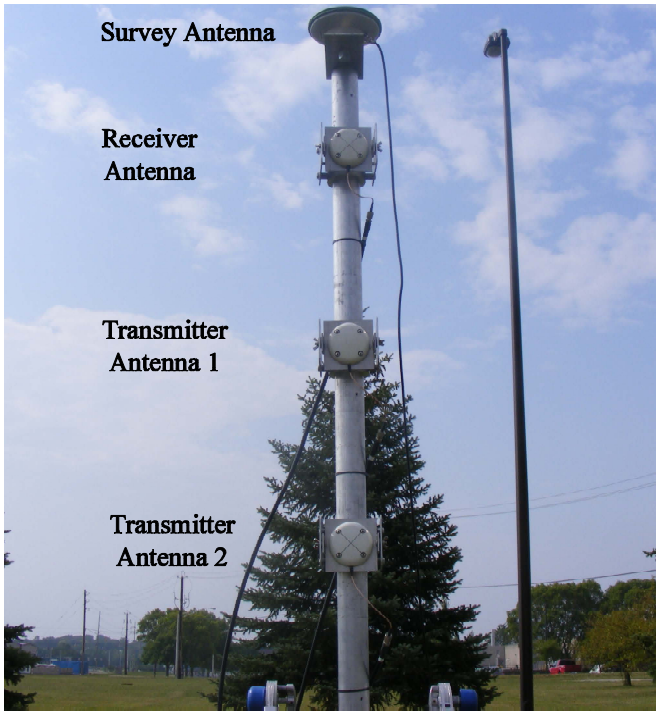

Figure 3.4: Pseudolite Tower Setup using Patch Antennas.

Table 3.1: Pseudolite Tower Positions in the Local Navigation Frame (ENU)

Location	x_{ENU}(meters)	y_{ENU}(meters)	z_{ENU}(meters)
Tower 1	-106.19	1083.22	-21.22
Tower 2	-197.79	89.40	-4.03
Tower 3	-144.45	-559.81	1.47
Tower 4	336.95	-1377.71	3.23
Tower 5	526.80	-488.08	2.11
Tower 6	380.86	159.27	-0.43

this site for test allowed the towers to have a clear line-of-site to each other and the receiver for the majority of the trajectory.

3.4 Simulation Development

The use of simulations to test the failure detection algorithm was done so an accurate depiction of performance statistics could be generated. The simulations were developed using the test data from the field work. The inertial data used in the simulations was the same as the data used in the field experiments. Modifications were done to the measurement update data, where perfect carrier phase measurements were calculated based on the truth data. The truth data is calculated using NovAtel's Waypoint Post-Processing Software [23]. The simulated carrier phase measurements were based on adding different types of errors to perfect phase measurements. The errors can be separated into two different classes—instantaneous cycle slips and slow growing errors. On top of the cycle slips and the slow growing errors, white Gaussian noise was added to all carrier phase and pseudorange measurements. The variance of the phase noise was 1cm, while the pseudoranges have a variance of 2.5 meters. This is in line with the actual measurement noise value used in the R matrix.

Instantaneous cycle slips occur occasionally in the pseudolite carrier phase measurements. The magnitude of the cycle slips is in terms of wavelengths. The Locata pseudolite system can have cycle slips as small as a partial wavelength. Also a cycle slip occurs within one sample.

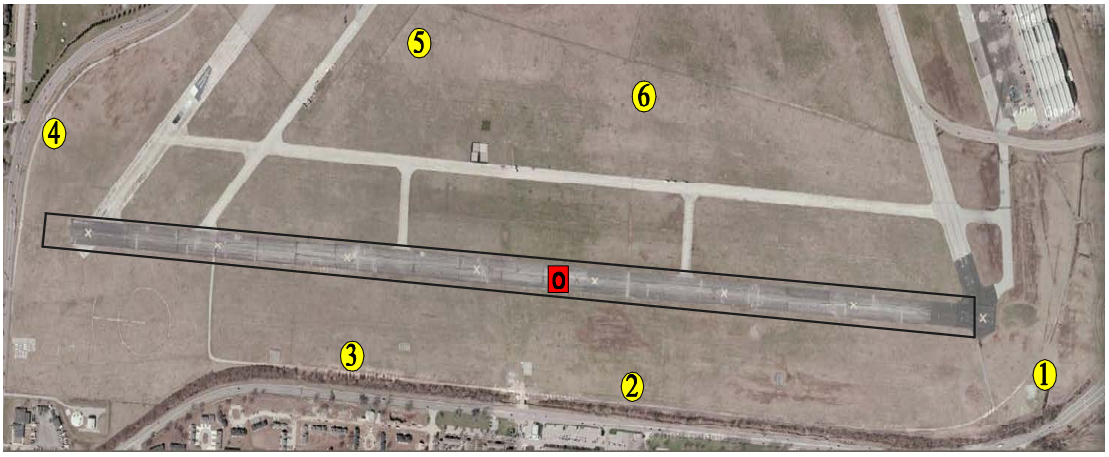

Figure 3.5: Pseudolite Tower Positions Relative to the Runway used for the Field Test.

Slow growing errors happen over a number of measurement samples. These type of errors are characterized by the slope of the growth of the error. In this research, slope will be defined as the number of wavelengths the error grows per sample.

3.5 Summary

This section discussed the techniques used to detect and remove failures in a pseudolite navigation system. The pseudolite navigation system is integrated with the inertial sensor to provide a navigation estimate to compare individual carrier phase measurements over time to detect failures such cycle slip and slow growing errors. The local level inertial error model was implemented in the extended Kalman filter algorithm. The navigation filter was developed using error states with the extend Kalman filter algorithm. Updates to the filter were single difference pseudolite carrier phase measurements. The next section will present the results of the filter described above using the field experiment and simulations.

IV. Results of Navigation Filter

This chapter presents the results of two failure detection algorithms implemented in a pseudolite and inertial base navigation filter. The first section presents the errors that were modeled in this research, using real pseudolite phase measurements. The second section describes the details of the field test, such as the trajectory, pseudolite locations, and the truth source. The simulations are based on the truth source of the field test. The third section discusses the results of the residual monitoring failure detection algorithm using simulated measurements that contain errors. The fourth section presents the performance of the moving window failure detection algorithm using simulations. The statistics used to characterize each scenario in the simulations include the failure detection rate, false alarms, and the number of samples required to detect an error. The navigation results from the field test using the pseudolite measurements and inertial data are shown in the fifth section.

4.1 Single Difference Observables

The carrier phase measurements in a pseudolite system contain errors that are modeled in two ways—instantaneous cycle slips and slowly growing errors. Instantaneous cycle slips occur in a similar fashion as the GPS case were the system loses tracking lock and the ambiguity changes as a result. The slow growing errors, which may or may not lead to cycle slips, occur over multiple samples. A slow growing error that ramps up (increases in error) then ramps down (decreases in error) can be seen in Figure 4.1. The single differenced error (SD Error) in Figure 4.1 was calculated by differencing the carrier phase measurements from PRN 1 and PRN 11. The true range was removed using the true navigation solution obtained by carrier-phase-based DGPS. A closer look, given in Figure 4.2 shows the slowly growing error that is being focused on in this research. This error grows over a series of samples, finally reaching an error of -1 meter. The error then ramps back down to

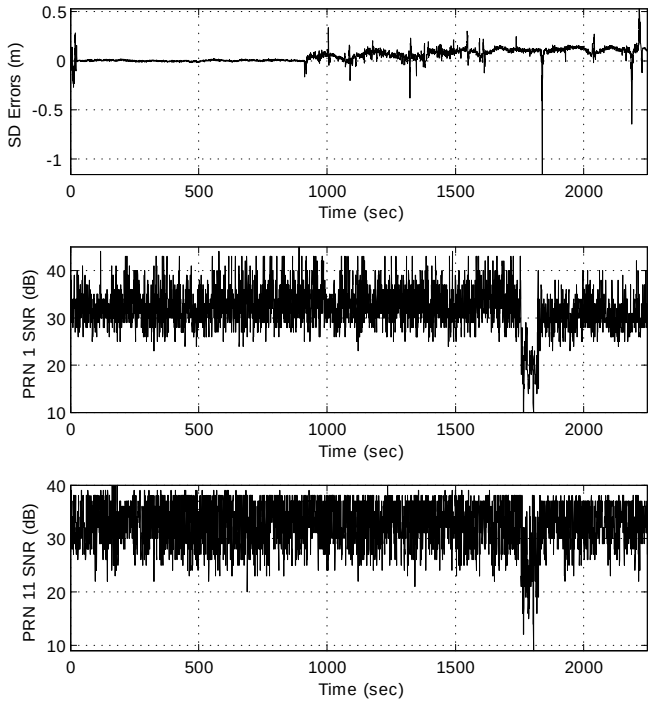

Figure 4.1: The Single Differenced Error with the True Range Removed, shown with the Corresponding SNR Measurement. The Measurement shown is from PRN 1 and 11.

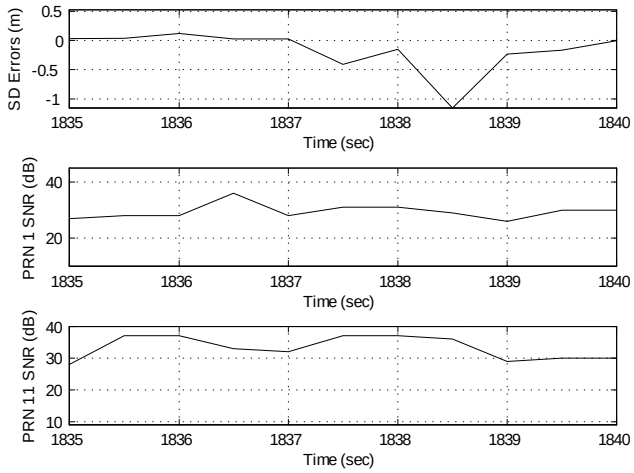

Figure 4.2: A Closer View of a Slow Growing Error in the Single Differenced Carrier Phase Ambiguity. The Measurement shown is from PRN 1 and 11.

zero over another series of samples. Also shown in the figure are the SNR values for each PRN used to calculate the single difference measurement. The SNR does dip before the time the error occurs but does not appear to be related to the actual slow growing error. During the time of the error both signals have an SNR measurement of approximately 30dB.

The pseudolite phase measurements also contain large cycle slips such as the ones shown in Figure 4.3. Figure 4.3 shows the single differenced error between PRNs 1 and 11. The cycle slips in the single differenced ambiguity occur several times over the period of the field test. Figure 4.3 shows the SNR measurements are relatively stable when the cycle slips occur. These cycle slips lead to the requirement of a failure detection algorithm that is independent of SNR measurements.

4.1.1 Cycle Slip Detection (SNR-based). Past work used the signal-to-noise ratio to determine cycle slips in the pseudolite phase measurements [1] [30]. One of the assumptions made when using the SNR technique is that a cycle slip could still occur when the SNR is above the set threshold. The research done here shows that cycle slips can occur even when the SNR is relatively high. The SNR technique does

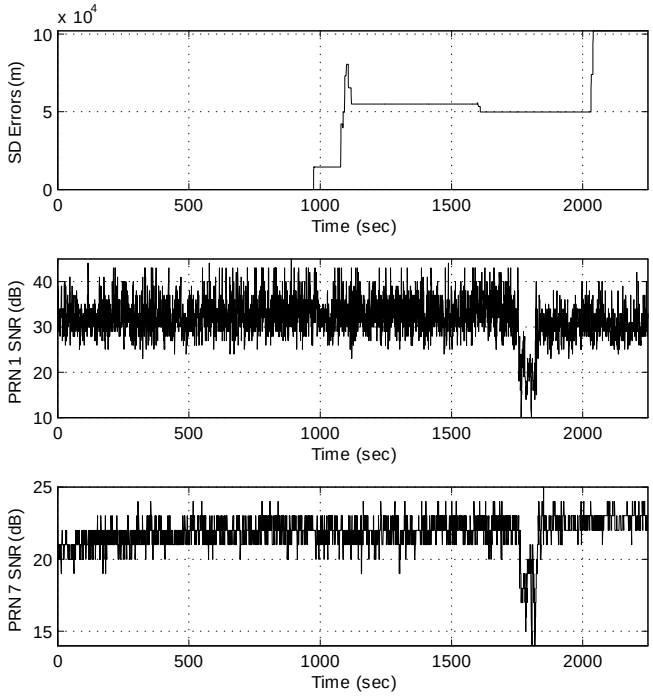

Figure 4.3: A Single Differenced Ambiguity Containing Large Cycle Slips, shown with SNR Measurements. The Single Differenced Measurement is based on PRN 1 and 7.

not address cycle slips caused by other means when the SNR is normal, above the set threshold, such as the case shown in Figure 4.2. The past work used 8dB as the cutoff threshold for the cycle slip detection [30]—however, data collected for this works shows that the power levels rarely drop below this threshold. It should also be noted that the Locata receivers used for this research were updated between the previous work [30] and this current research.

4.2 Field Test

4.2.1 Navigation Trajectory. The field test section is based on the trajectory shown in Figure 4.4, which will be referred to as the area B runway test. The location of the field experiment was an old runway located on area B at Wright-Patterson AFB. A golf cart, containing the navigation sensors, was used as the test vehicle (Section 3.4). The navigation path was relatively flat, with less than 10 meters of variation in the local vertical axis. The average velocity when moving was approximately 4 m/s.

4.2.2 Geometry of the Pseudolite Network. The pseudolite reference system was installed along the runway, shown in Figure 4.4 and described in Section 3.4. Figures 4.5 and 4.6 shows the corresponding position and velocity of the trajectory over time. The vehicle was at rest for a lengthy period at the start of the trajectory and also came back to rest at the end of the period. One issue when using a ground-based reference system is the impact the geometry of the measurements has on the position solution. To show the geometry impacts the dilution of precision (DOP) was calculated. Two DOP measurements are used to describe the geometry, horizontal dilution of precision (HDOP) and vertical dilution of precision (VDOP). DOP is the RMS error for the least squares position solution caused by 1 meter of RMS error in the measurements [9].

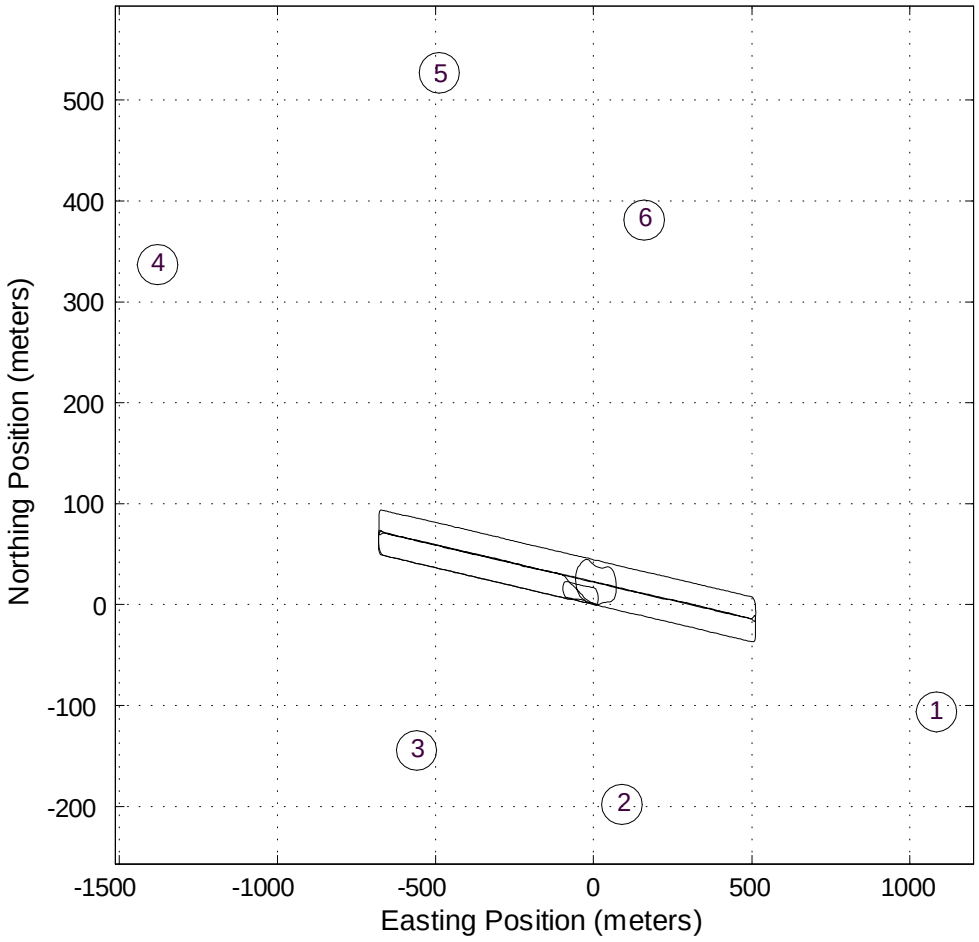

Figure 4.4: Area B Runway Test Trajectory shown Relative to the Pseudolite Tower Locations.

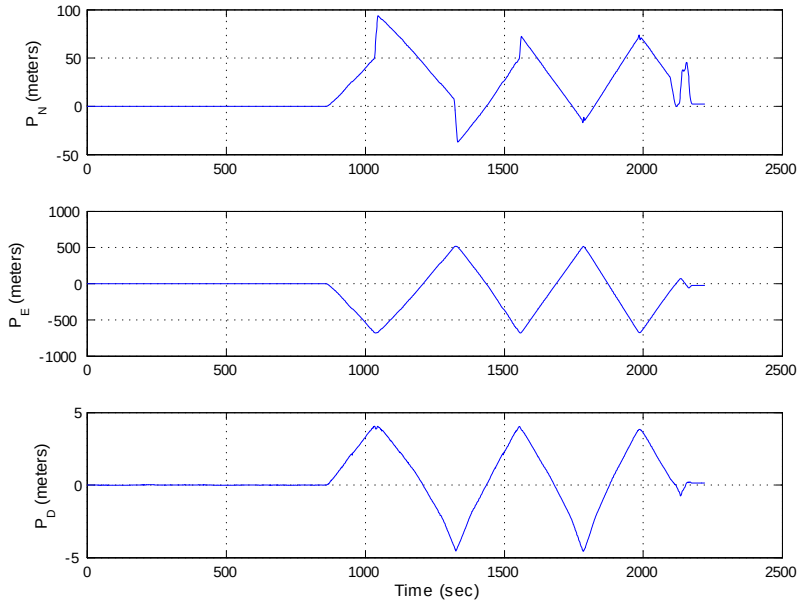

Figure 4.5: Position in the NED-Frame is shown for the Navigation Period of the Area B Runway Test.

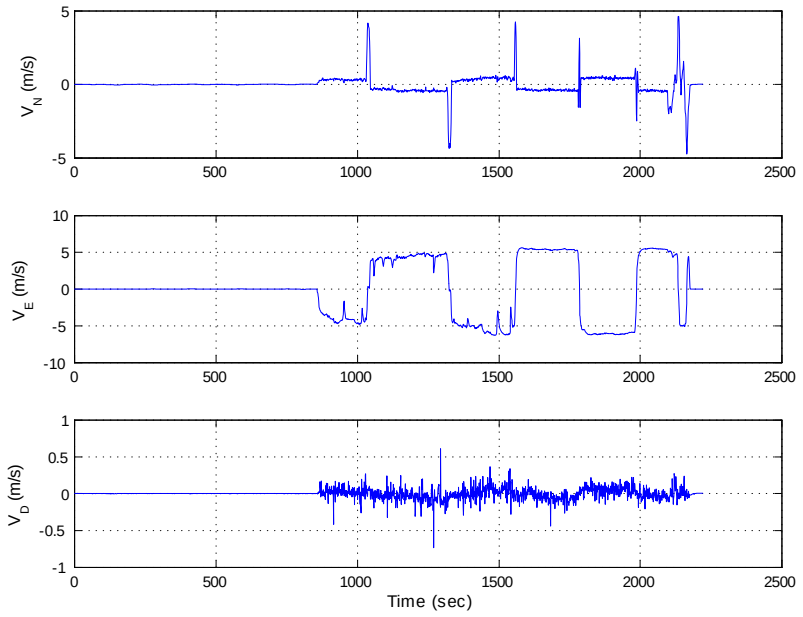

Figure 4.6: Velocity in the NED-Frame is shown for the Navigation Period of the Area B Runway Test.

The HDOP and VDOP are based on the sensitivity matrix (H) for the single difference carrier phase measurements. The first step is to calculate the DOP matrix D.

$$D = (H^T H)^{-1} \tag{4.1}$$

The diagonal terms of the DOP matrix are used to calculate the DOP values. For the case of HDOP the first two diagonal terms are used, representing the x and y directions in the local frame.

$$HDOP = \sqrt{D_{11} + D_{22}} \tag{4.2}$$

For the VDOP the third diagonal term of the DOP matrix (D) is used. The VDOP is based on the error in the vertical direction of the local frame.

$$VDOP = \sqrt{D_{33}} \tag{4.3}$$

More detail on DOP can be found in [21].

The horizontal geometry is very good, as shown in Figure 4.7. The RMS horizontal position error is expected to be $10 - 25$cm, based on the HDOP and the error in a single difference carrier phase measurement, which is approximately 10cm. The RMS error in the vertical channel will be approximately $6 - 15$ meters, based on the VDOP shown in Figure 4.7. The Kalman filter however will reduce the weighting of the measurements when applying corrections to the vertical channel [9].

4.3 Simulation Results for Residual Monitoring Failure Detection

This section will show the results of the residual monitoring failure detection algorithm, based on simulated errors in simulated pseudolite measurements. Simulations are used in this work so errors could be analyzed in more detail. The ability to navigate using real data is important, but the errors in real data are a combina-

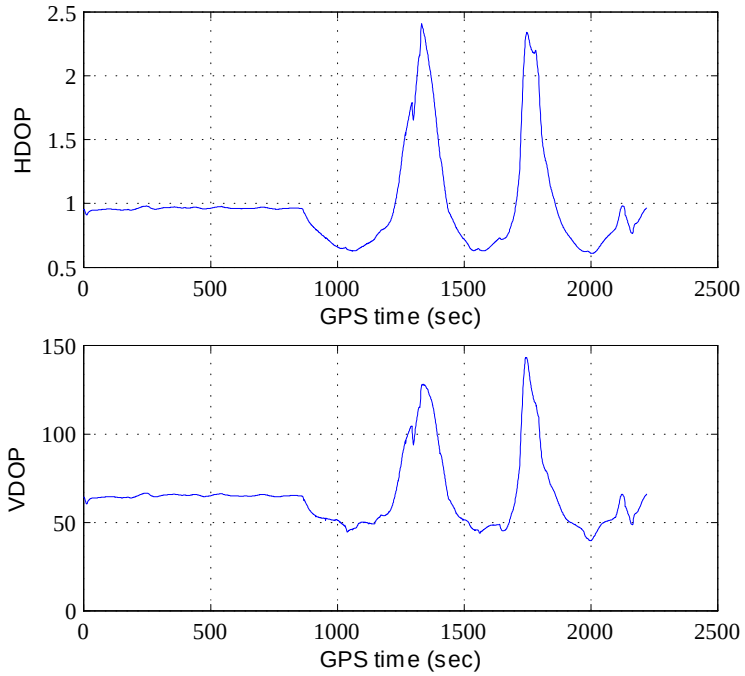

Figure 4.7: HDOP and VDOP based on the Pseudolite Network and Navigation Trajectory.

tion of many factors. Simulations are necessary to validate the actual performance of the failure detection algorithms. The simulations are based on using the true carrier phase and true range measurements calculated from the true positions based on DGPS. The true position was solved using NovAtel's Waypoint Inertial Explorer Post-Processing Software [23]. The pseudolite measurement update rate for the simulations was set to 2Hz.

Two types of simulated errors were added to the true carrier phase measurements. These errors included instantaneous cycle slips and slow growing errors. In addition to these errors, white Gaussian noise was added to the true range measurements and the simulated phase measurements. Instantaneous cycle slips are characterized as errors that occur between samples. Cycle slips can be any magnitude and occur randomly in real measurements. In the simulation the size of the cycle slip errors was varied from 0.5λ to 10λ, with a step size of 0.5λ. This range of wavelengths is where the detection algorithm's performance varies depending on the

likelihood function and inertial sensors used. A sample of a cycle slip was shown in Figure 4.3. The second type of error analyzed in the simulations was the addition of slow growing errors to the phase measurements. A slow growing error is characterized by the amount the error grows over a number of samples. The slow growing error occurred over 10 samples in all the simulations. This type of error is based on the real pseudolite phase measurements, as seen in Figure 4.2. The slow growing error rate was varied from $0.5\frac{\lambda}{samp}$ to $10\frac{\lambda}{samp}$. The step size was $0.5\frac{\lambda}{samp}$ for each simulation.

4.3.1 Truth Source. The simulated measurements are based on a truth source. The quality of the truth data will impact the simulation results. Figure 4.8 shows the 2DRMS of the estimated horizontal position error, based on the estimated standard deviations provided by the Waypoint Post-Processing Software [23]. The 2DRMS was calculated using $\sqrt{\sigma_n^2 + \sigma_e^2}$ [21]. The GPS data and the HG1700 inertial data were used to produce this solution. The average 2DRMS was approximately 1.5cm. The accuracy of the true navigation solution will aid in the calculating of the true pseudolite measurements. Large variations of error in a truth source will cause false detections in the failure detection algorithm.

4.3.2 Instantaneous Cycle Slips. In this set of simulations, the true carrier phase measurements were combined with instantaneous cycle slips and measurement noise. The simulations are based on the field experiments, so 20 carrier phase signals were created. Instantaneous cycle slips were added to 4 of the 20 signals. The starting points of each of the simulated errors were offset by 15 samples—this was done so the errors did not occur at the same time in multiple signals. The simulated cycle slips were added every 200 samples. An example of one set of simulated cycle slips is shown in Figure 4.9. In this example the cycle slip magnitude is 2 wavelengths. Also a total of 25 cycle slips were added to this one signal. The sign of the cycle slip was randomly assigned. The phase measurement update rate was 2Hz for a total

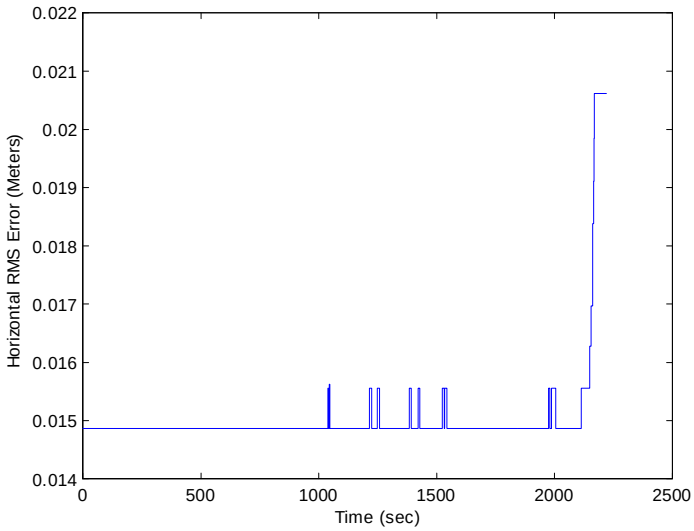

Figure 4.8: Truth Source RMS Error (reported by Waypoint Post-Processing Software).

of 4440 updates in this simulation. The simulation was repeated varying the size of the cycle slip error from 0.5λ to 10λ, in increments of 0.5λ. The results using a 3σ threshold and a 2.5σ threshold for the residual monitoring failure detection algorithm are shown below.

The first simulation based on instant cycle slips used a failure detection threshold of 3σ. For the residual distribution, 99.7% of the residuals should lie within 3σ, since the residual estimation is based on a normal distribution [20]. The failure detection rate for both inertial sensors, shown in Figure 4.10, tends to be as expected. The detection rate increases as the size of the errors grow. With the 3σ threshold the HG1700 system does not achieve 100% detection until the errors are 3.5λ and larger. The MIDG requires even larger errors (5.5λ) to achieve until full detection.

The average detection delay using a 3σ threshold to detect cycle slips is shown in Figure 4.11. Detection delay is defined as the number of samples the error is allowed to be incorporated into the filter before being rejected by the failure detection algorithm. The detection delay is reported only when the errors were large enough

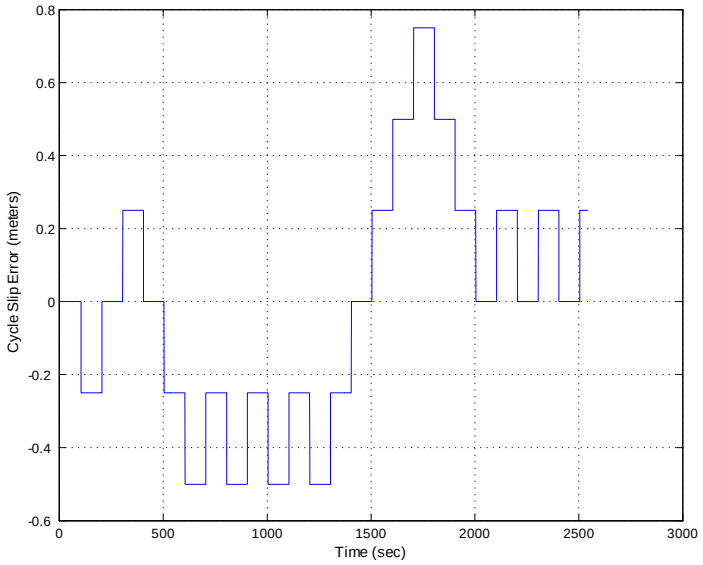

Figure 4.9: An Example of Simulated Cycle Slips with a Magnitude of 2λ.

for the failure algorithm to detect errors. A spike occurs when the algorithm begins to find some errors but it takes the filter a number of samples to detect them. As the magnitude of the cycle slip errors grow, the delay reaches zero. The HG1700 is capable of quickly detecting errors, as shown in Figure 4.11. The false alarms for both inertial systems are shown in Figure 4.12. Since the threshold was set to 3σ, the number of false alarms were relatively low in both cases. The 2DRMS horizontal position error is shown in Figure 4.13. The RMS error of the HG1700 system maintained a fairly consistent 2DRMS position error of approximately 20cm. The MIDG had large fluctuations of error in the position estimates. This error was caused by not detecting the cycle slips. When the errors are small (less than a wavelength) they do not cause a large amount of position error. The RMS error grows as the cycle slip errors grow in size and the MIDG failure detection algorithm misses detection.

The threshold of the residual monitoring method was decreased to 2.5σ, since a large number of small (less than 3 wavelengths) cycle slip errors were not detected using either IMU. The detection rate for the 2.5σ threshold is shown in Figure 4.14.

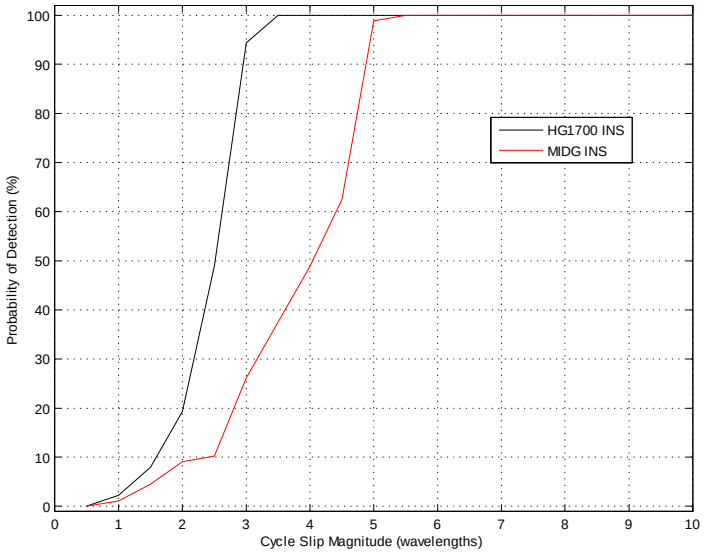

Figure 4.10: Detection Rate for the Residual Monitoring Failure Detection Algorithm, with Instant Cycle Slips (3σ threshold).

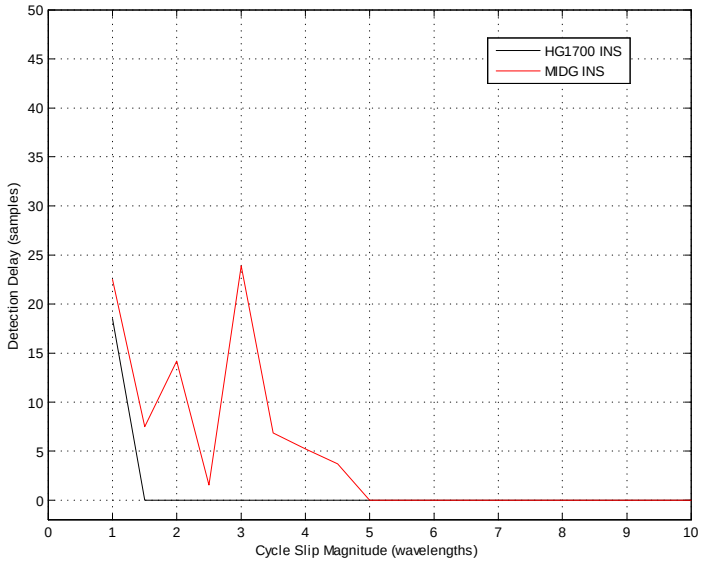

Figure 4.11: Detection Delay for the Residual Monitoring Failure Detection Algorithm, with Instant Cycle Slips (3σ threshold).

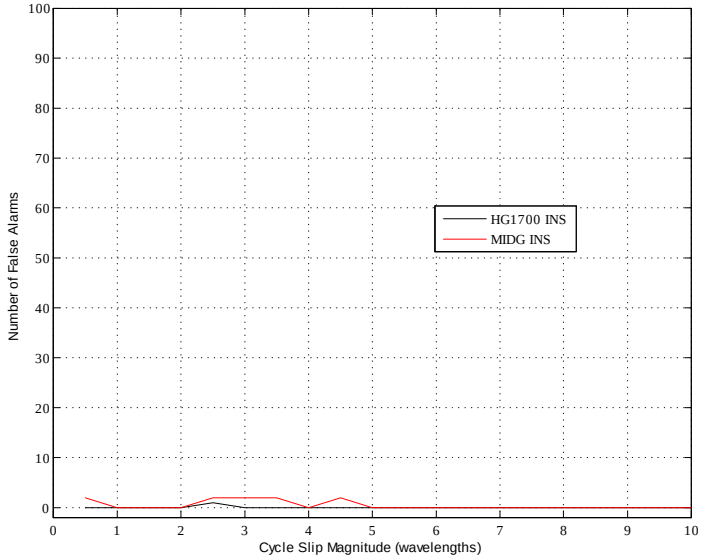

Figure 4.12: False Alarms for the Residual Monitoring Failure Detection Algorithm, with Instantaneous Cycle Slip Errors (3σ threshold).

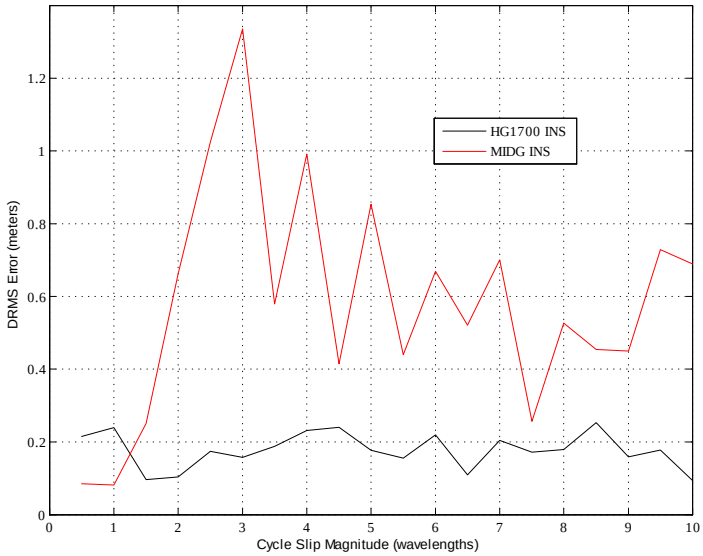

Figure 4.13: 2DRMS Position Error for the Residual Monitoring Failure Detection Algorithm, with Instantaneous Cycle Slip Errors (3σ threshold).

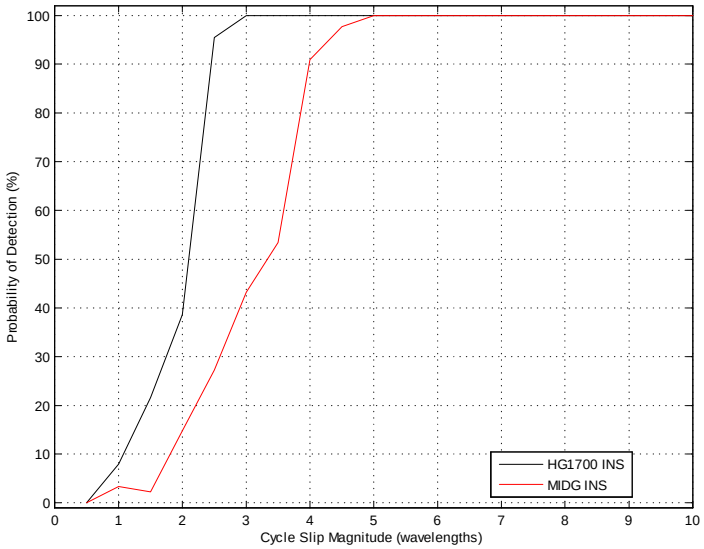

Figure 4.14: Detection Rate for the Residual Monitoring Failure Detection Algorithm, with Instant Cycle Slips (2.5σ threshold).

Reducing the threshold to 2.5σ made it possible to detect 100% of the 3λ cycle slips, for the HG1700, and 5λ, for the MIDG. The detection delay for the same case is shown in Figure 4.15. The detection delay, in the case of the MIDG, decreased for cycle slips that are 3λ and larger. The HG1700 delay decreased significantly (from 18 samples to 3 samples), in the case of 1 wavelength cycle slips. The false alarms are shown in Figure 4.16. There were zero false alarms for the HG1700 case. This is a small improvement, since there was only one false alarm using the 3σ threshold. The false alarms of the MIDG increased significantly from the 3σ case. This is caused by a combination of the smaller threshold and missed detections causing error in the filter estimates. The 2DRMS horizontal position error is shown in Figure 4.17. The error overall is reduced in both cases. The HG1700 maintains an accuracy of less than 20cm. The MIDG has less error using the 2.5σ threshold when the cycle slips are 3λ and larger. Figure 4.17 shows how the large number of false alarms increases the 2DRMS in the case of the MIDG.

Using a smaller threshold (2.5σ) allowed the filter to detect and remove the cycle slip errors at a higher probability, when compared to the 3σ threshold results.

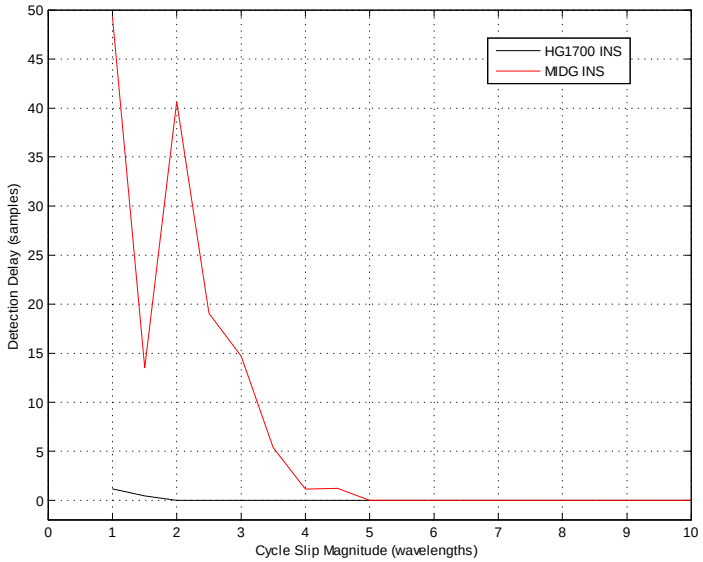

Figure 4.15: Detection Delay for the Residual Monitoring Failure Detection Algorithm for Instant Cycle Slips (2.5σ threshold).

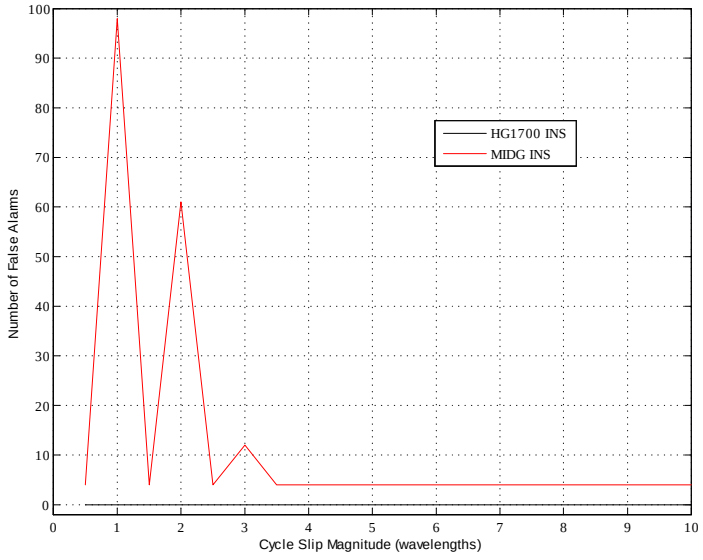

Figure 4.16: False Alarms for the Residual Monitoring Failure Detection Algorithm, with Instantaneous Cycle Slip Errors (2.5σ threshold).

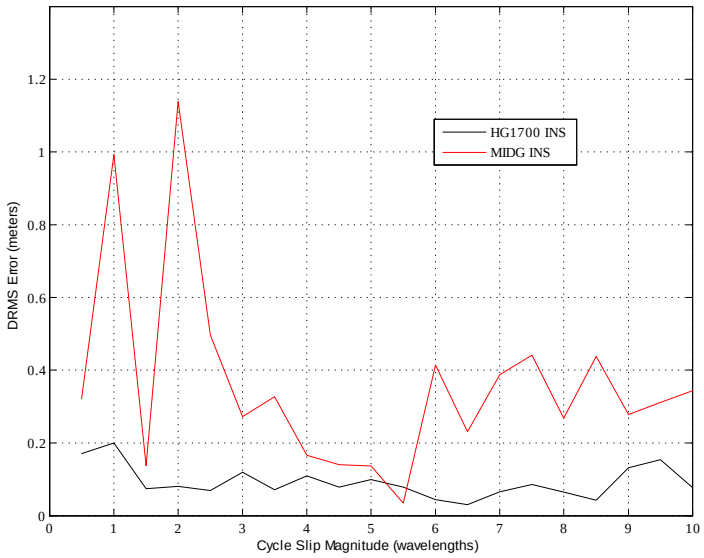

Figure 4.17: 2DRMS Position Error for the Residual Monitoring Failure Detection Algorithm, with Instantaneous Cycle Slip Errors (2.5σ threshold).

Higher detection rates lead to the increased position accuracy when using the 2.5σ threshold, with both inertial systems. The residual monitoring method is appropriate for detecting cycle slips as small as 3λ, when using the HG1700 IMU.

4.3.3 Slow Growing Error Detection. Slow growing errors grow over a period of multiple samples. The slow growing errors were simulated to occur over a 10 sample period. An example of the simulated slow growing errors is shown in Figure 4.18. In this example the error rate is $2\frac{\lambda}{samp}$, thus the errors grow to approximately 2.5 meters over 10 samples. Also in this example only four of the slow growing errors are shown in the figure below. The slow growing errors were added to the true phase measurement every 100 samples, for a total of 49 slow growing errors on each of the four designated signals. The simulations consist of using 20 carrier phase measurements at a time, the same as the field test work. Four of these twenty signals contain slow growing errors. The statistics below are based on the entire set of samples for each run. The inertial-based navigations systems are

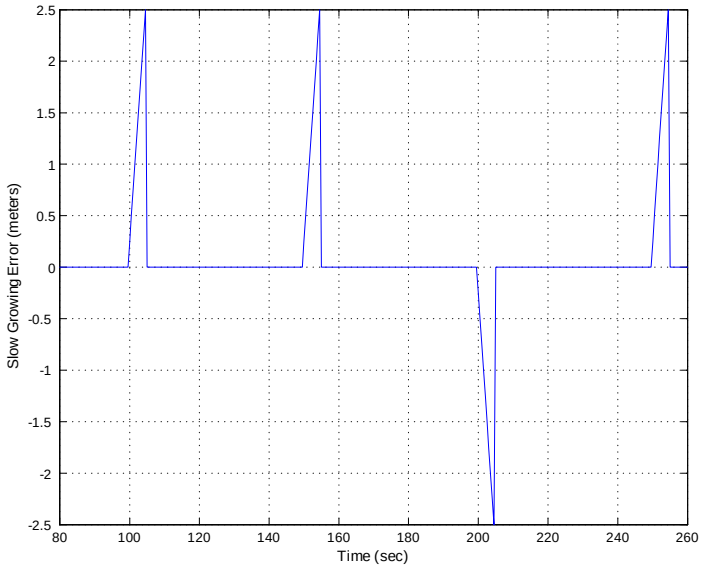

Figure 4.18: An Example of a Simulated Slow Growing Errors with a Growth Rate of 2 $\frac{\lambda}{samp}$.

compared through common characteristics—the detection rate, the detection delay, and the false alarms in each subset.

The first set of simulations using the slow growing errors used a 3σ threshold in the residual failure detection algorithm. The detection rates for the HG1700 and MIDG are shown in Figure 4.19. Both sensors had high detection rates for even small errors. The detection delays for this case of slow growing errors are shown in Figure 4.20. The delay in the detections was significant with both IMUs for the $0.5\frac{\lambda}{samp}$ error.

The HG1700 has a detection delay larger than 1 sample for errors that grow less than $3\frac{\lambda}{samp}$. The MIDG delays are more profound, since the 1 sample detections do not start until the error growth rate reaches $5\frac{\lambda}{samp}$. During the delays, the errors are being incorporated into the filter estimates. In this simulation, the filter does not diverge since the errors only occur in 4 of the 20 signals. The false alarms are shown in Figure 4.21. There are no false alarms when using the HG1700 with a 3σ threshold. The 2DRMS horizontal position error is shown in Figure 4.22.

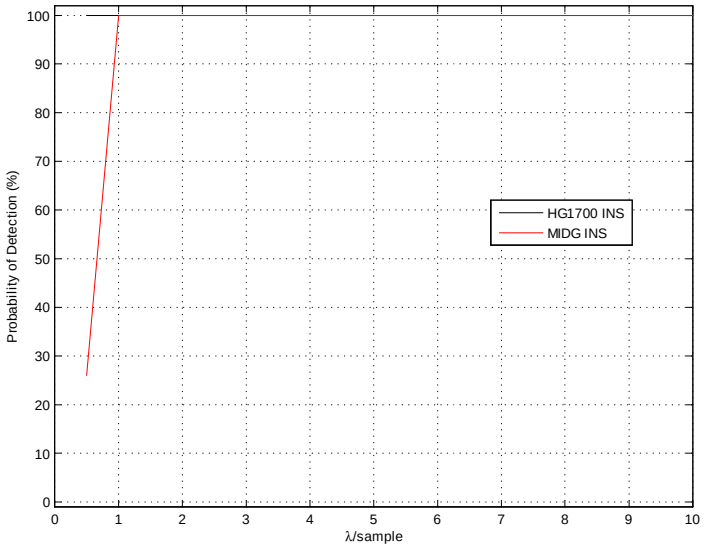

Figure 4.19: Detection Rate for Residual Monitoring Failure Detection Algorithm in the Case of Various Slow Growing Error Rates (3σ threshold).

The position estimates from the MIDG navigation filter were double the size as the HG1700 navigation filter.

The idea was to reduce the threshold to 2.5σ to try to reduce the number of samples required to detect the failure. The detection rates for this case are shown in Figure 4.23. The detection rates remain the same except for one exception, the MIDG increased to a 80% detection rate in the $0.5\frac{\lambda}{samp}$ case. The HG1700 does have a slightly faster detection time for the case $0.5\frac{\lambda}{samp}$, shown in Figure 4.24. The slow growing error simulation has shown the MIDG can detect small growing errors well when using a 2.5σ threshold. The false alarms are shown in Figure 4.25. The MIDG False alarms increased for all the measurements. There is a false alarm consistent with all the simulations—this is most likely due to a slight variation from one epoch to the next in the truth data. The 2DRMS horizontal position error is shown in Figure 4.26. Reducing the threshold leads to more accurate position estimates using both IMUs.

Reducing the threshold increases the accuracy of the MIDG navigation filter. A small amount of the position estimate improvement in the two cases can be con-

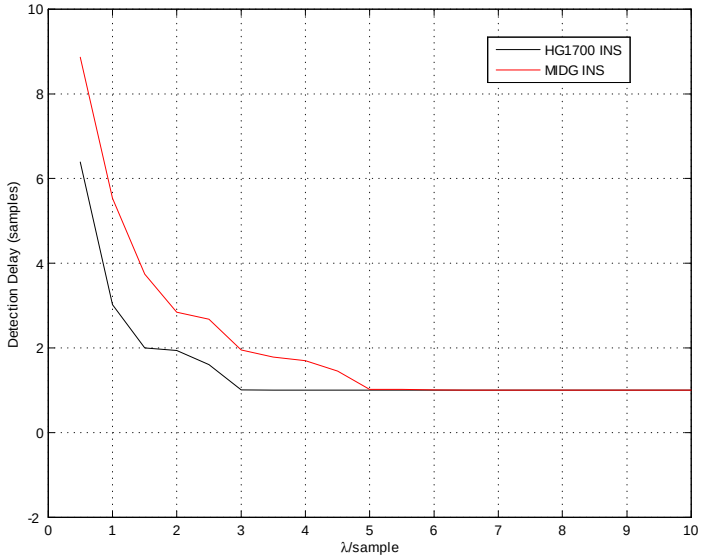

Figure 4.20: Detection Delay for Residual Monitoring Failure Detection Algorithm in the Case of Various Slow Growing Error Rates (3σ threshold).

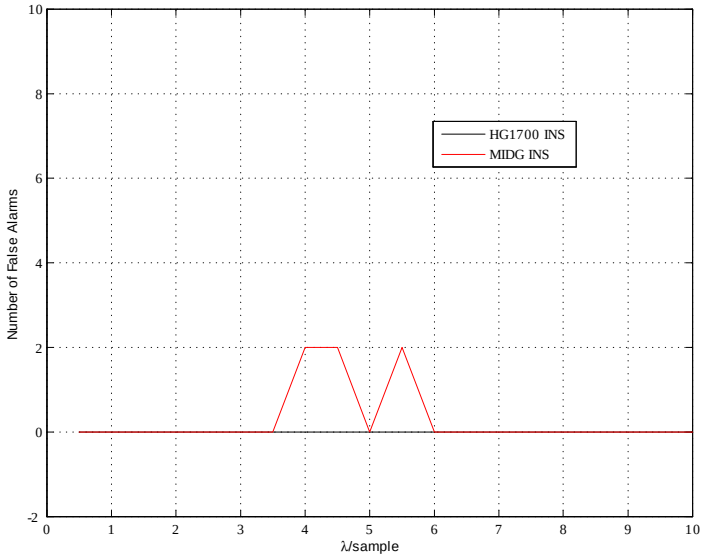

Figure 4.21: False Alarms for Residual Monitoring Failure Detection Algorithm in the Case of Various Slow Growing Error Rates (3σ threshold).

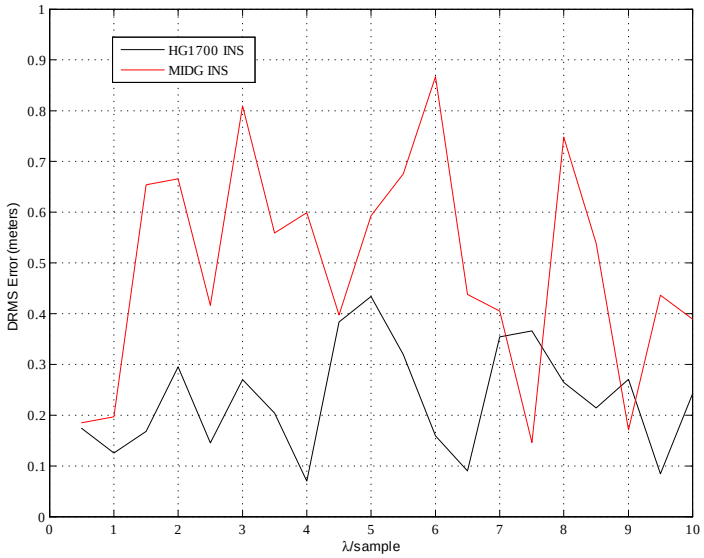

Figure 4.22: 2DRMS Position Error for Residual Monitoring Failure Detection Algorithm in the Case of Various Slow Growing Error Rates (3σ threshold).

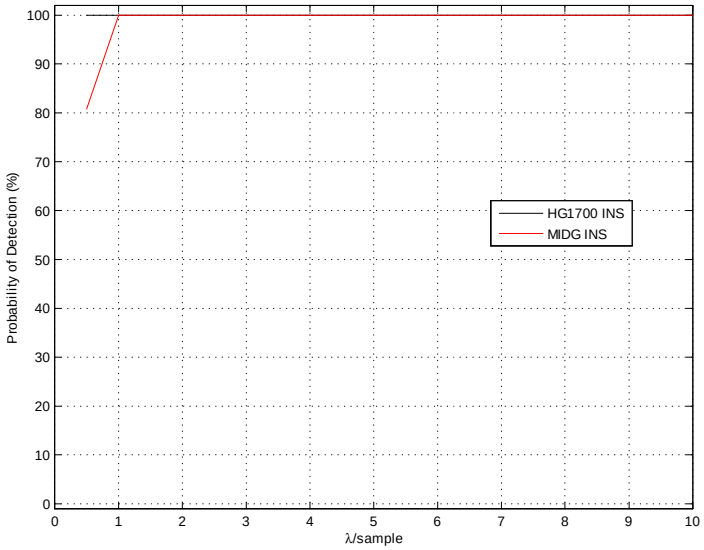

Figure 4.23: Detection Rate for Residual Monitoring Failure Detection Algorithm with Various Slow Growing Error Rates (2.5σ threshold).

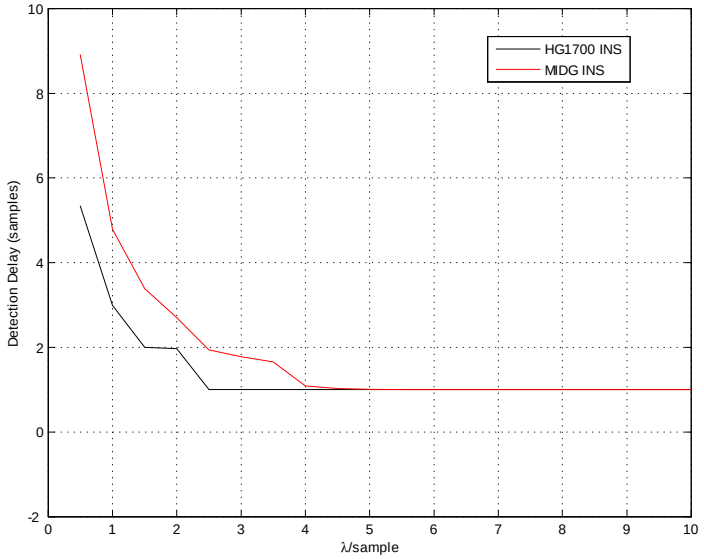

Figure 4.24: Detection Delay for Residual Monitoring Failure Detection Algorithm with Various Slow Growing Error Rates (2.5σ threshold).

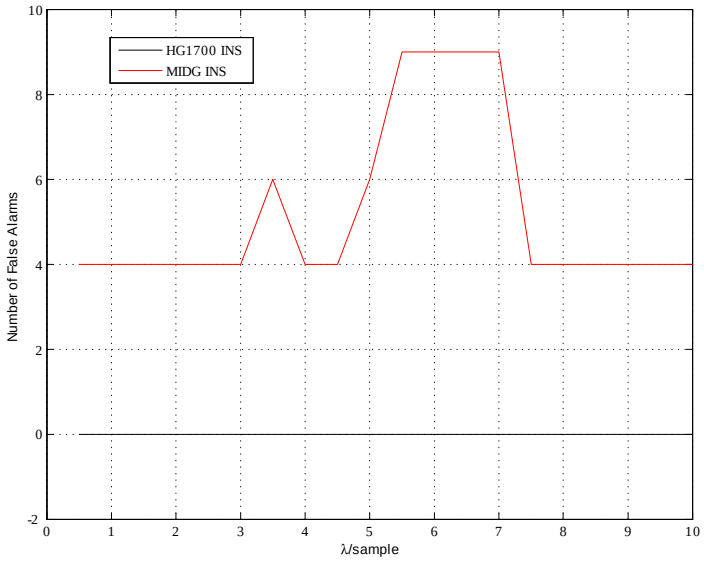

Figure 4.25: False Alarms for Residual Monitoring Failure Detection Algorithm with Various Slow Growing Error Rates (2.5σ threshold).

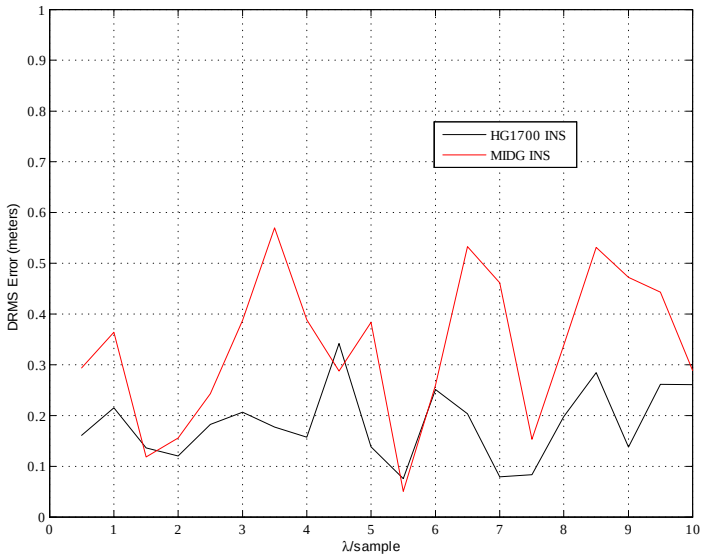

Figure 4.26: 2DRMS Position Error for Residual Monitoring Failure Detection Algorithm with Various Slow Growing Error Rates (2.5σ threshold).

tributed to the random nature of how the simulation data was created. The random noise of the pseudorange measurements can impact the estimated position, since the pseudoranges are used to re-initialize the ambiguities. The pseudoranges have an error variance of 2.5 meters. Overall the position estimates are better with the 2.5σ threshold—this is due to faster detections.

4.4 Testing the Moving Window Failure Detection using Simulations

This section focuses on the results of using a moving window failure detection algorithm to detect simulated errors. The moving window likelihood function described in Section 3.3.2 was implemented using both INS navigation systems, the MIDG and the HG1700. There are two cases that were simulated using the moving window method. The first analyzed the instantaneous cycle slips, while the other focused on the slow growing errors. Simulations in this section were developed and conducted in the same fashion as the ones in Section 4.3. The threshold for the moving window function was the same for both of the cases that were simulated.

4.4.1 Instantaneous Cycle Slips. The first set of simulations analyzed instantaneous cycle slips errors in the carrier phase measurements. The detection rates shown in Figure 4.27 can be compared with the residual monitoring (2.5σ threshold) technique shown in Figure 4.14. The HG1700 and MIDG can achieve 100% detection rate for cycle slips of 2 and 3.5 wavelengths, respectively, when using the moving window method. This is an improvement over the residual monitoring technique for both IMUs.

One issue with the moving window algorithm was that the detection delay, shown in Figure 4.28, increased over the residual monitoring technique (from Figure 4.10). The detection delay for the MIDG increased for the very small cycle slips, which is shown in Figure 4.28. The delay in detection using the window method for the HG1700 increased overall. The HG1700 had significant detection delays for detecting cycle slips smaller than 3λ, when compared to the residual method with the 2.5σ threshold (shown in Figure 4.15). In general, the windowing method requires more samples to detect a failure. This is due to the algorithm of the windowing function.

The False alarms are shown in Figure 4.30. The false alarms for the MIDG are much higher using the window method then the residual monitoring technique. The large delay in detection and the high number of false alarms cause errors in the navigation solution for the MIDG system. The position error DRMS for both systems is shown in Figure 4.29. The HG1700 maintains better than 15cm of horizontal position error. The MIDG error varies over the test period, reaching as high as 70cm of DRMS position error.

The MIDG was capable of more accurate position estimates using the window method compared to the residual monitoring technique, as seen by comparing Figures 4.17 and 4.29. This is driven by the higher detection rates when using the moving window method. The HG1700 was also capable of more accurate position estimates with cycle slips of 1λ and less, when using the window method. The window method

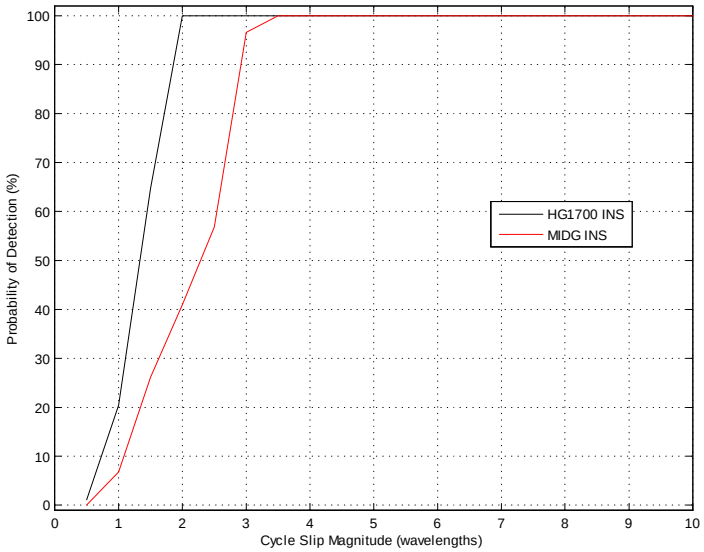

Figure 4.27: Detection Rates when using Moving Window Failure Detection Algorithm, with Cycle Slip Errors.

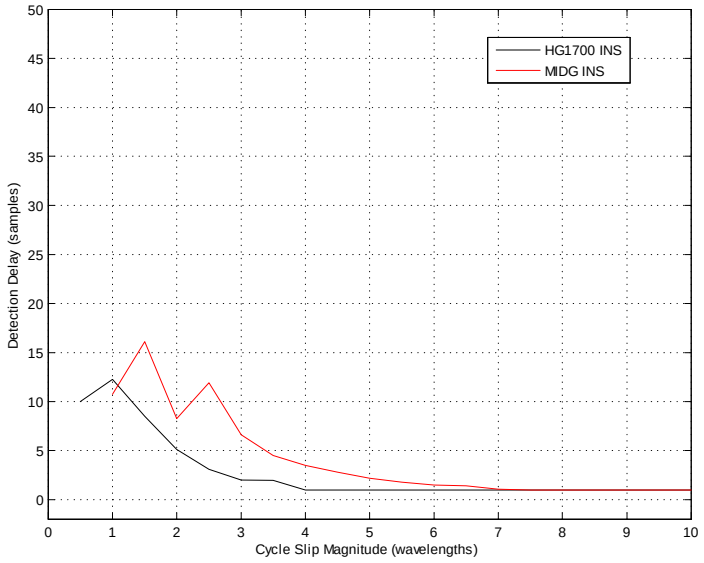

Figure 4.28: Detection Delay when using Moving Window Failure Detection Algorithm, with Cycle Slip Errors.

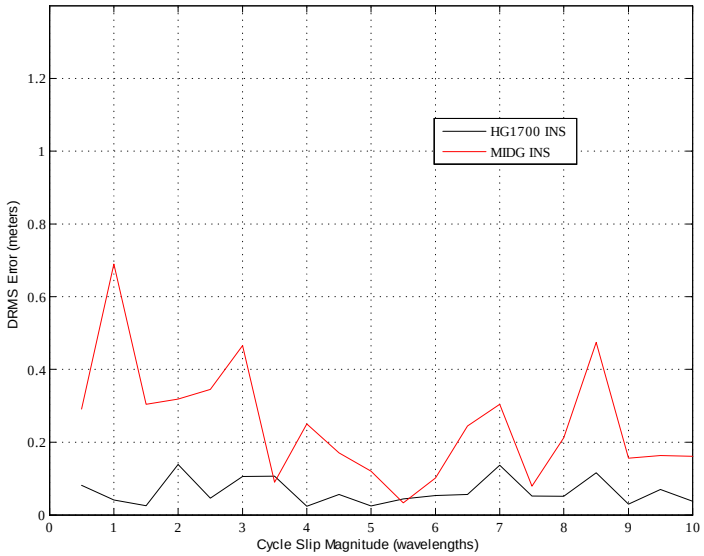

Figure 4.29: 2DRMS Position Error when using Moving Window Failure Detection Algorithm, with Cycle Slip Errors.

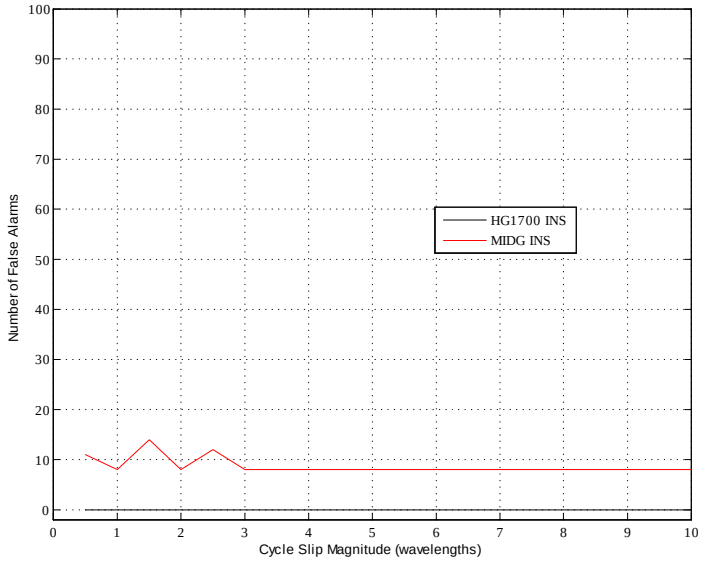

Figure 4.30: False Alarms for the Detection of Cycle Slips, using the Moving Window Failure Detection Algorithm.

does attain higher detection rates than the residual method, but also can have a small delay. From these results the small delay does not seem to impact the overall position error.

4.4.2 Slow Growing Error Detection. The second case of analyzing the moving window method was to test the algorithm by simulating slow growing errors. The errors were added to the true phase measurements in the same manner as described in Section 4.3. The probability of detection is shown in Figure 4.31. The probability of detecting $0.5\frac{\lambda}{samp}$ errors for the MIDG was nearly 99% when using the window failure detection algorithm. This is an increase in detection of 19% from the residual monitoring method.

The delay of detection for both IMUs never hits 1 sample, shown in Figure 4.32. The detection delay is due to the moving window algorithm. When there is a failure present, the moving window algorithm surpasses the threshold approximately one sample later than the residual monitoring technique.

The 2DRMS position error of the MIDG system (Figure 4.33) reached as much as 40cm. The HG1700 position error 2DRMS was above 20cm on three occasions (Figure 4.33). This error for both systems stems from the inability of this technique to detect 100% of the failures, with the smallest possible delay, and no false alarms.

In Figure 4.34, the false alarms for both inertial systems is shown. The HG1700 has zero false alarms over the course of the cases tested. The MIDG has several false alarms at each case. These false alarms occurred in the same location for each simulation run when using the MIDG inertial data. The inertial data of the MIDG estimates the phase measurements inaccurately at the specific interval, causing the false alarms.

The moving window function detected a higher rate of failures than the residual monitoring method, for the smallest of small growing errors. The windowing function

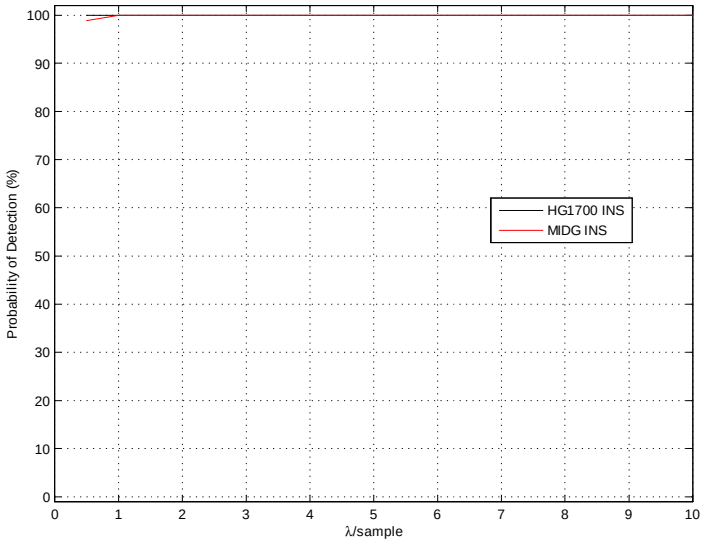

Figure 4.31: Detection Rates when using Moving Window Failure Detection Algorithm, with Slow Growing Errors.

does have a small delay. This is most likely due to the 10 samples the window method uses to calculate the likelihood.

4.5 Field Test Navigation Results

The true trajectory was calculated from the GPS measurements using NovAtel's Waypoint Post-Processing Software [23]. Waypoint provided an estimated RMS accuracy of 2cm or less in horizontal position error and 4cm or less in vertical position error. The attitude information used as the truth data for the field test was from the NovAtel Black Diamond System (BDS). Both inertial sensors were used to process the navigation data twice. The first run used the residual monitoring failure detection algorithm, while the second run used the moving window function as the failure detection algorithm. The threshold for the residual monitoring failure detection algorithm was set to 3σ. This threshold gave the best results in terms of RMS position error.

The position error for pseudolite carrier phase navigation and residual monitoring algorithm, using the HG1700 IMU, is shown in Figure 4.35. The true position

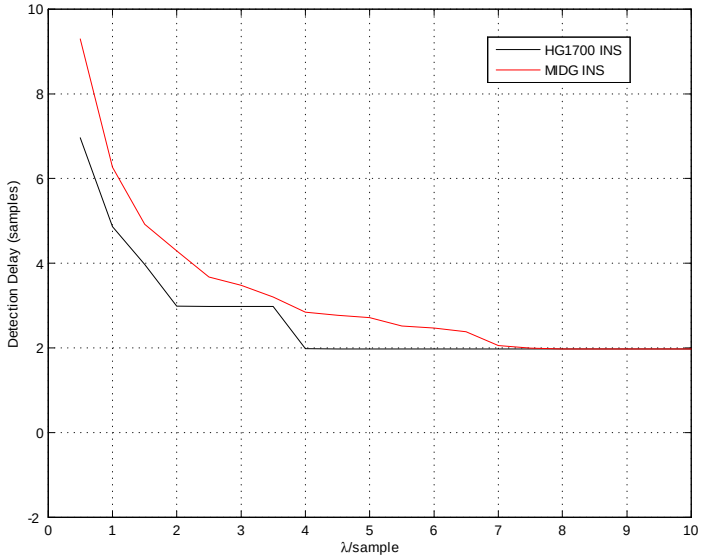

Figure 4.32: Detection Delay when using Moving Window Failure Detection Algorithm, with Slow Growing Errors.

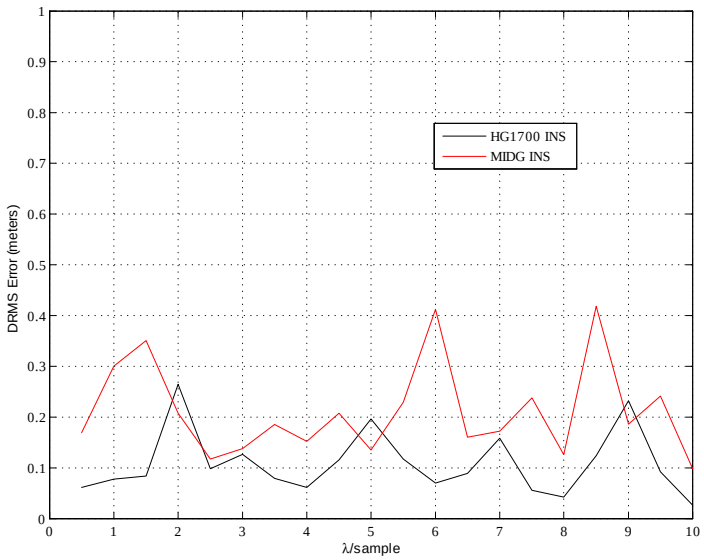

Figure 4.33: 2DRMS Position Error when using Moving Window Failure Detection Algorithm, with Slow Growing Errors.

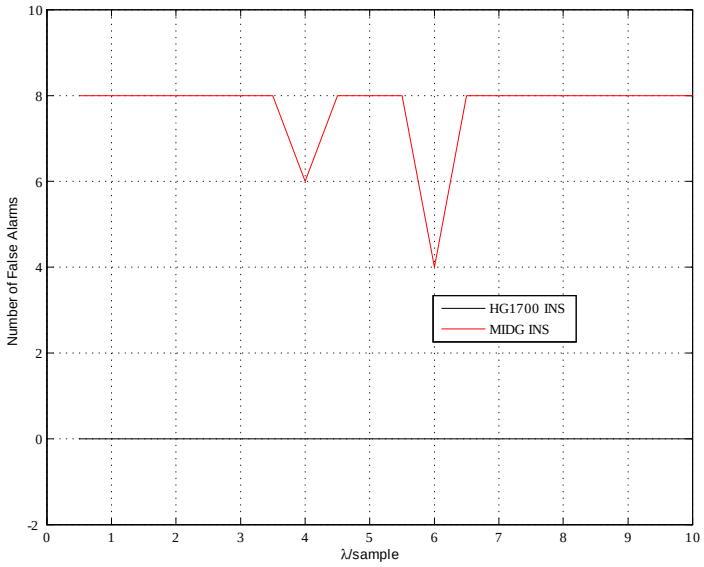

Figure 4.34: False Alarms for the Detection of Slow Growing Errors, using the Moving Window Failure Detection Algorithm.

error is bounded by the estimated 1σ standard deviation of the error. The position errors for the pseudolite/MIDG navigation system are shown in Figure 4.36. The trajectory in Figure 4.4 was used in both cases.

The position errors of the navigation system using the moving window failure detection algorithm are shown below. Figure 4.37 shows the results when using the HG1700, while Figure 4.38 shows the position errors when using the MIDG IMU. Both figures include the estimated 1σ bound of the position errors.

The navigation position errors for each case are shown in Table 4.1. The HG1700 provided an improvement of around 2-3cm over the MIDG in horizontal positioning. The errors between the two failure detection algorithms were similar, with some small variations. The moving window function performed better than the residual monitoring failure detection when using the HG1700. The residual monitoring was slightly better than the moving window when using the MIDG. The moving window function performs best when residuals before the failure contain the

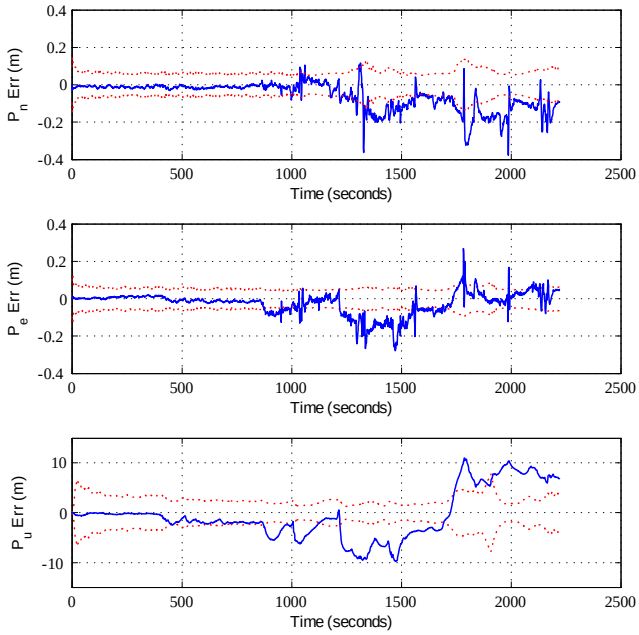

Figure 4.35: True Position Error shown in the NED Frame for the HG1700 based Navigation System (Blue). The Residual Monitoring Failure Detection Algorithm was use in this Case. The Estimated 1σ Error Bound is shown in Red.

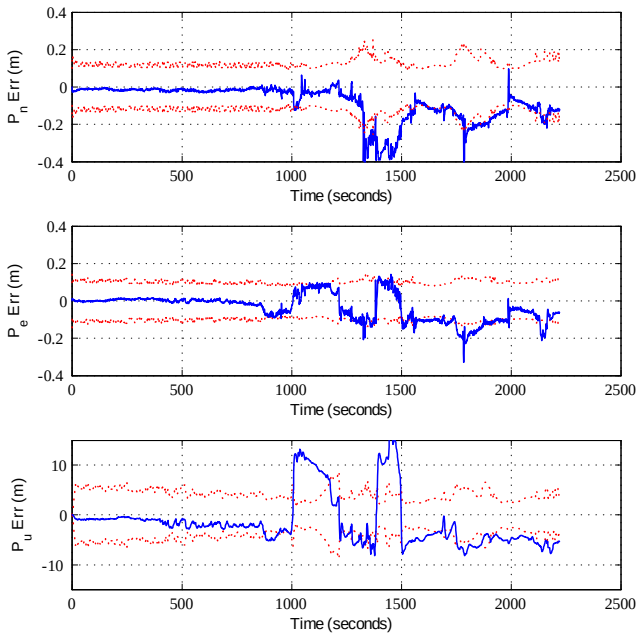

Figure 4.36: True Position Error shown in the NED Frame for the MIDG Based Navigation System (Blue). The Residual Monitoring Failure Detection Algorithm was use in this Case. The Estimated 1σ Error Bound is shown in Red.

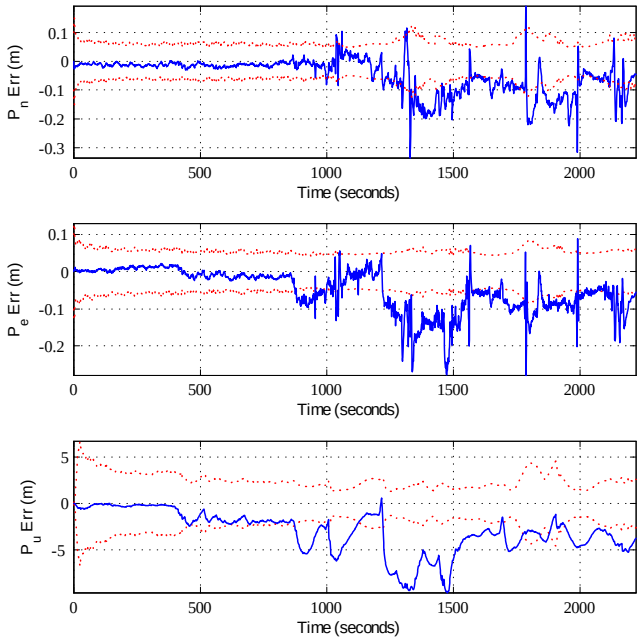

Figure 4.37: True Position Error shown in the NED Frame for the HG1700 based Navigation System (Blue). The Likelihood Function was the Moving Window Algorithm. The Estimated 1σ Error Bound is shown in Red.

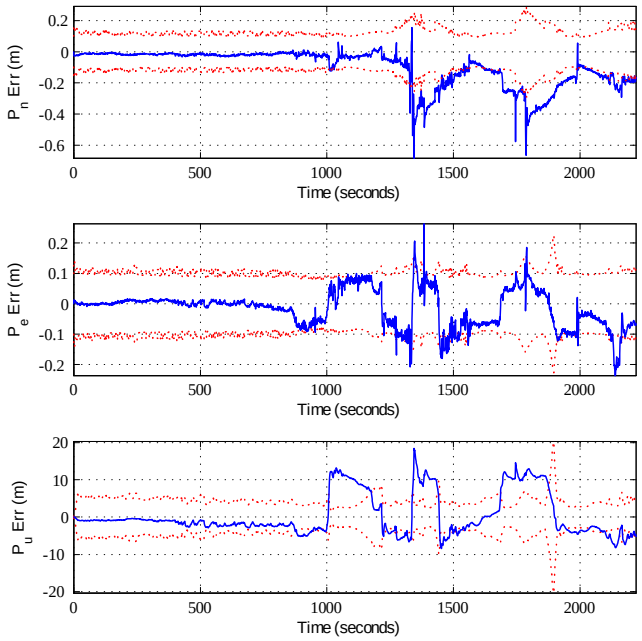

Figure 4.38: True Position Error shown in the NED Frame for the MIDG Based Navigation System (Blue). The Likelihood Function was the Moving Window Algorithm. The Estimated 1σ Error Bound is shown in Red.

Table 4.1: RMS Position Error of Navigation Filter in Real Data using Multiple Failure Detection Scenarios

Failure Detection Algorithm	Position Error	HG1700	MIDG
Residual Monitoring	2DRMS (m)	0.08	.105
	3DRMS (m)	2.89	3.08
Moving Window	2DRMS (m)	0.077	.117
	3DRMS (m)	2.22	3.26

least error. The HG1700 produces lower residuals then does the MIDG, causing the window method to work better with the HG1700.

4.5.1 Failure Detection in the Pseudolite Measurements. The single difference pseudolite measurement availability is shown in Figure 4.39. The available measurements are shown in green, while the rejected measurements are shown in the black. The rejected measurements were detected using the failure detection algorithm, in this case the residual monitoring based algorithm. The coverage plot shows a large number of rejections for multiple observations (1, 3, 8, 17, and 19)—this is due to a combination of two issues. The first issue was that these signals did not go into phase lock until approximately 900 seconds into the navigation period. During this time the phase measurements were oscillating, thus the failure detection algorithm was working as it should by rejecting the phase measurements as cycle slips. The second issue was that once the signals were in phase lock their corresponding ambiguity was not accurately initialized causing the single difference measurement to be rejected at each epoch. This issue stems from the roll-over correction that was made to the pseudorange measurements, causing the initialization of the ambiguities to be inaccurate. The coverage plot also shows observations 17, 18, and 19 do not provided coverage after 1700 seconds. The cause of the coverage to drop from these measurements was due to power loss in the number 6 pseudolite tower.

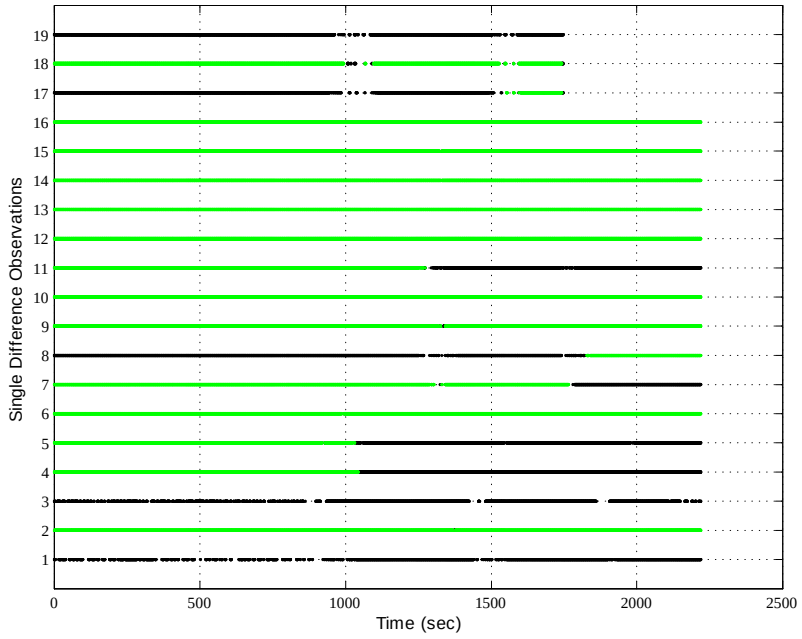

Figure 4.39: The Pseudolite Coverage from the Area B Runway Test. The Failure Detections of the Single Difference Observations are shown in Black. The Valid Single Differenced Pseudolite Measurements are shown in Green.

4.6 Combined Failure Detection Algorithm

The residual monitoring technique has been shown to have faster failure detections then the moving window method overall. But the moving window algorithm was able to detect smaller errors at a higher probability then the residual monitoring method. This leads to the idea of combining both failure detection methods to detect the highest number of failures with the highest probability. This could be done by using the multiple model approach laid out in Section 2.8.

The residual monitoring technique should be implemented with an aggressive threshold (e.g., 2σ) that will increase the capability to detect small errors. This will lead to a number of false alarms that can be mitigated by using the moving window algorithm as the hypothesis test to determine if a failure actually occurred in a filter. Using this technique should increase the ability to detect smaller cycle slips and slow growing errors more accurately.

4.7 Summary

Discussed in this chapter was the implementation and results of two different failure detection algorithms. The algorithm experiments were derived from both field tests and simulation work. Each case was presented to show the statistical characteristics of performance. These statistics consisted for detection rate, detection delay, and false alarms. Both failure detection algorithms were shown to be able to detect cycle slips and slow growing errors in the pseudolite carrier phase measurements. This chapter also showed that using a failure detection algorithm with a MIDG inertial sensor can achieve decimeter accuracy when integrated with a pseudolite positioning system.

V. Conclusion

5.1 Overview

This thesis presented two methods for detecting failures in pseudolite phase measurements. The purpose of a failure detection algorithm is to detect and remove cycle slips and slow growing errors that commonly occur in pseudolite phase measurements. This effort was inspired by past work that relied on the SNR measurements to detect cycle slips. The removal of cycle slips and slow growing errors improves the reliability and accuracy of the pseudolite measurements.

The first failure detection method used a residual monitoring approach to determine if a failure occurred. In this method a set threshold (number of standard deviations) was used to evaluate the residual and declare a failure. The second method used a moving window function to detect errors in the update step of the filter algorithm. The moving window uses a predefined number of samples (N) to evaluate the likelihood of a failure. Each sample is based on the ratio of the residual and variance. This method depends on the previous residuals as well as the current residual.

The navigation system consisted of a pseudolite network and an inertial sensor integrated through an error state extended Kalman filter. The update measurements of the pseudolite system were in the form of single differenced observables. Two different inertial sensors, a Honeywell HG1700 and a Microbotics MIDG II, were used in the filter to analyze the impact of inertial quality in determining failures.

Implementing a navigation reference system in a field experiment showed the capability of the failure detection algorithm to identify and remove the errors in actual phase measurements and achieve decimeter accuracy. The navigation reference system consisted of the pseudolite and inertial sensors, plus a GPS reference receiver. The truth source was calculated using NovAtel's Waypoint Post-Processing

Software [23]. Developing simulations based on this data allowed the algorithms to be characterized down to the performance of each inertial sensor.

5.2 Conclusions

Integrating a pseudolite-based network with inertial measurements is an effective way of detecting cycle slips. The tightly integrated pseudolite and inertial measurements led to the ability to detect and remove the errors in the carrier phase measurements. Once the cycle slips are detected the ambiguity for that corresponding measurement is re-initialized to the new value. The residual monitoring technique to determine the failures proved to be an accurate and effective method. The residual monitoring method is considered effective in the sense that the algorithm used information available in the Kalman filter to detect and remove errors in raw pseudolite measurements, such as the cycle slips and slow growing errors. This increased the reliability in the navigation system. This is the first step in developing the integrity of a pseudolite system.

Failure detection performance was improved by all measures when using the higher quality INS. A higher quality IMU will measure the trajectory more precisely in between updates, thus calculating the residual more precisely and providing the failure detection algorithm a more accurate estimation of the errors in the measurements. This was shown through the use of the HG1700 IMU. The comparison of the two inertial sensors revealed that the Honeywell HG1700 outperforms the Microbotics MIDG in terms capability to detect failures. The MIDG is capable of detecting cycle slips and slow growing errors when using a failure detection algorithm, but the HG1700 was able to detect a higher rate of failures in fewer samples.

The residual monitoring method was able to detect cycle slips more quickly than the moving window algorithm. Comparing the detection delays of the residual monitoring method shows the HG1700 was capable of detecting slow growing errors

of $2.5\frac{\lambda}{samp}$ and larger in one sample, while the moving window algorithm could not detect any errors in one sample for the same scenario.

The threshold for the residual monitoring failure detection algorithm performed best when set to 2.5σ. The MIDG did have a number of false alarms when using the 2.5σ threshold, but had higher detection rates and required less samples to detect a failure. In the end, the HG1700 performed effectively using a 2.5σ threshold. The simulation results showed the HG1700 performed very well in both algorithms that were implemented. The HG1700 was limited to detecting the instant cycle slips of 3 wavelengths and larger, when using the residual monitoring method.

The moving window method was able to detect more cycle slips than the residual monitoring method. The detection rate of cycle slips with a magnitude of 3 wavelengths, when using the MIDG, increased from 54%, when using the residual monitoring technique, to 95%, when using the moving window method. The moving window function was capable of detecting instantaneous cycle slips of 1.5 wavelengths at 96% when using the HG1700, where only 20% were detected when using the residual monitoring method.

There are many issues when using the moving window technique as the likelihood function in the failure detection algorithm. The windowing method uses N number of previous residuals, thus noise and other errors tend to contribute to the likelihood of failure value. This can lead to false alarms as seen when using a lower quality IMU such as the MIDG.

The results in this research have lead to the idea of using a combined failure detection approach to maximize the capabilities of detecting errors. In this approach the residual monitoring algorithm would be used to detect the failures quickly. While the moving window algorithm would then be used to confirm there was a failure through a multiple model approach, as explained in Section 4.6.

5.3 Recommendations

Implementation of the failure detection algorithms in this work has increased the reliability and accuracy of the pseudolite-based reference system. Some improvements to the failure detection algorithm could improve the ability to detect smaller errors. Removing the errors will in turn lead to a more accurate navigation solution. The following areas could build on this work for improving the pseudolite referencing system:

- Explore the benefits of using a navigation grade IMU, such as the HG-764. Increasing the accuracy of the navigation solution in the propagation state can make the detection of smaller errors possible.
- Develop a technique to quantify the integrity of the pseudolite-based navigation system.
- Implement a failure detection algorithm that uses both the residual monitoring method and the moving window function. This could be done in a multiple model approach such as described in Section 4.6.
- Implementation of a multiple model failure detection approach would be the next algorithm to implement. In this concept, the idea is to run a new filter based on a hypothesis of failure detection, while keeping the original filter. Running both filters in parallel will continue until one diverges or is proven to be true through a hypothesis test. Overall this should do two things—assure the filter does not diverge and keep the inertial measurements from causing false detections. The quality of the inertial sensor has had a large impact on the failure detection, as seen in the false alarms of the MIDG. Using a filter algorithm that spawns a new filter at each failure could reduce the impact of false alarms. The failure detection in each filter can use the residual monitoring technique laid out in this work, although other methods could also be implemented.

Bibliography

1. Amt, John. *Methods for Aiding Height Determination in Pseudolite-Based Reference Systems Using Batch Least-Squares Estimation.* MS thesis, Air Force Institute of Technology, March 2006.

2. Amt, John and John Raquet. "Flight Testing of a Pseudolite Navigation System on a UAV," *ION NTM*, 1147–1154 (2007).

3. Babu, Ravindra and Jinling Wang. "Ultra-Tight Integration of Pseudolites with INS," *IEEE*, 705–714 (2006). Sydney, Australia.

4. Barnes, Joel, Chris Rizos, Mustafa Kanli, Amnuj Pahwa, David Small, Gavin Voigt, Nunzio Gambale, and Jimmy Lamance. "High Accuracy Positioning using Locata's Next Generation Technology," *ION GPS/GNSS 2005* (2005).

5. Barnes, Joel, Chris Rizos,Jinling Wang, David Small, Gavin Voigt, and Nunzio Gambale. "Locata: A New Positioning Technology for High Precision Indoor and Outdoor Positioning," *ION GPS/GNSS* (September 2003).

6. Barnes, Joel, Chris Rizos,Jinling Wang, David Small, Gavin Voigt, and Nunzio Gambale. "Locata: The Positioning Technology of the Future," *SatNav* (July 2003). The 6th International Symposium on Satellite Navigation Technology Including Mobile Positioning and Location Services.

7. Bhatti, Umar. "An Improved Sensor Level Integrity Algorithm for GPS/INS Integrated System," *ION GNSS*, 3012–3023 (September 2006). 19th International Technical Metting of the Satellite Division.

8. Bouska, Terry and John Raquet. "Development and Simulation of a Pseudolite-Based Flight Reference System," *ION NTM* (January 2004). San Diego, CA.

9. Brown, Robert and Patrick Wang. *Introduction to Random Signals and Applied Kalman Filtering.* New York, New York: John Wiley and Sons, 1997.

10. Changdon, Kee, So Hynoungmin, Kim Jeonghan, Jun Haeyoung, Per Enge, and Sam Pullen. "Effect of the Error in the Line-of-Sight Unit Vector on Pseudolite-Based Positioning Systems," *ION NTM* (January 2004). San Diego, CA.

11. Crawford, Matthew. *Optimal Geometric Deployment of a Ground Based Pseudolite Navigation System to Track a Landing Aircraft.* MS thesis, Air Force Institute of Technology, June 2006.

12. Gray, Robert and Peter Maybeck. "An Integrated GPS/INS/Baro and Rada Altimeter System for Aircraft Precision Approach Landings." Air Force Institute of Technology.

13. Henzler, Jens and Martin Weiser. "Using Pseudolite as A Flightlanding System," *ION 55th Annual Meeting*, 199–207 (June 1999). Cambridge, MA.

14. Huddle, James. *Advantages of Autonomous Integrity Monitored Extrapolation for Precision Approach*. Technical Report, Northrop Grumman.

15. Islam, Najmul, Elena Simona Lohan, Elina Pajala, Markku Renfors, Abdelmonaem Lakhzouri, and Heikki Laitinen. "Indoor Fading Distributions for GPS-based Pseudolite Signals," *IEEE* (2007).

16. Kao, Wei-Wen and Chin-Lang Tsai. "Carrier Phase Indoor Positioning using Pseudolites and INS," *ION GPS/GNSS*, 2593–2598 (September 2003). Portland, OR.

17. Lawrence, Robert, Capt Jeremiah Shockley, Derek Ruff, Brent Neal, and Matthew Alsleben. "CIGTF Enhanced Precision Reference Systems," *American Institute of Aeronautics and Astronautics* (2007).

18. Lee, Hung Kyu. "GPS/Pseduolite/SDINS Integration Approach for Kinematic Applications," *ION GPS/GNSS* (September 2002). Portland, OR.

19. Maybeck, Peter S. *Stochastic Models, Estimation, and Controls Volume 2*. New York, New York: Academic Press, 1982.

20. Maybeck, Peter S. *Stochastic Models, Estimation, and Controls Volume 1*. Arlington, Virginia: Navtech Book and Software Store, 1994.

21. Misra, Pratap and Per Enge. *Global Positioning System Signals, Measurements, and Performance*. Lincoln, Massachusetts: Ganga-Jamuna Press, 2001.

22. National Imagery and Mapping Agency. *Department of Defense World Geodetic System 1984 - Its Definition and Relationships with Local Geodetic Systems*. Technical Report 8350.2, St. Louis, MO: Department of Computer Science, Michigan State University, January 2000.

23. Novatel, "Waypoint Post-Processing Software," 2007. Version 7.80.

24. Parkinson, Bradford and James Spikler. *Global Positioning System: Theory and Applications Volume 1*. Washington, DC: American Institute of Aeronautics and Astronautics, 1996.

25. Petovello, Mark. "Kalman Filter Reliability Analysis Using Different Update Strategies." *CASI Annual General Meeting*. April 2003.

26. Petovello, Mark. *Real-Time Integration of a Tactical-Grade IMU and GPS for HIGH-Accuracy Positioning and Navigation*. PhD dissertation, University of Calgary, April 2003.

27. Petovello, M.G., M.E. Cannon, G. Lachapelle, A. Huang, and V. Kubacki. "Integration of GPS and INS Using Float Ambiguities with Application to Precise Positioning for JPALS," *ION NTM-04* (January 2004).

28. Petrovski, I., I. Surouvtcev, T. Petrovskaia, K. Okano, M. Ishii, H. Torimoto, K. Suzuki, M. Toda, and J. Akita. "Precise Navigation Indoor," *SICE Annual Conference*, 1739–1744 (August 2004). Sapporo, Japan.

29. Raquet, John, Tom Holden, Anthony Nash, Patrick Fenton, Gerard Lachapelle, Weigen Qiu, and C Pelletier. "Development and Testing of a Mobile Pseudolite Concept for Precise Positioning," *Division of the Institute of Navigation ION GPS*, *43*(2):817 – 826 (Summer 1995).

30. Shockley, Jeremiah. *Estimation and Mitigation of Unmodeled Errors for a Pseudolite Based Reference System.* MS thesis, Air Force Institute of Technology, March 2006.

31. Shockley, Jeremiah and John Raquet. "Estimation and Mitigation of Unmodeled Errors for a Pseudolite Based Reference System." Air Force Institute of Technology.

32. Titterton, David and John Wston. *Strapdown Inertial Navigation Technology.* Herts. SGl 2AY, United Kingdom: The Institution of Electrical Engineers, 2004.

33. Veth, Michael. *Fusion of Imaging and Inertial Sensors for Navigation.* PhD dissertation, Air Force Institute of Technology, September 2006.

34. Wang, Jianguo, Jinling Wang, David Sinclair, and Leo Watts. "High-Accuracy Airborne GPS/INS Positioning Augmented by Pseudolite," *ION NTM* (January 2006). Monterey, CA.

35. Wei, Wang, Liu Zongyu, and Xie Rongrong. "INS/GPS/Pseudolite Integrated Navigation for Land Vehicle in Urban Canyon Environments," *IEE Conference on Cybernetics and Intelligent Systems*, 1183–1186 (December 2004). Sapporo, Japan.

36. Wieser, Andreas, Mark Petovello, and Gerard Lachapelle. "Failure Scenarios to be Considered with Kinematic High Precision Relative GNSS Positioning," *ION GPS/GNSS* (September 2004). Long Beach, CA.

37. Zhang, H.T., M.G. Petovello, and M.E. Cannon. "Performance Comparison of Kinematic GPS Integrated with Different Tactical Level IMUs." *ION NTM*. January 2005.

REPORT DOCUMENTATION PAGE

Form Approved
OMB No. 074-0188

1. REPORT DATE *(DD-MM-YYYY)*	**2. REPORT TYPE**	**3. DATES COVERED** *(From – To)*
26-03-2009	Master's Thesis	June 2008 - March 2009

4. TITLE AND SUBTITLE

Failure Detection of a Pseudolite-Based Reference System Using Residual Monitoring

5a. CONTRACT NUMBER

5b. GRANT NUMBER

5c. PROGRAM ELEMENT NUMBER

6. AUTHOR(S)

Ciampa, Michael A., Capt, USAF

5d. PROJECT NUMBER
JON# 09-167

5e. TASK NUMBER

5f. WORK UNIT NUMBER

7. PERFORMING ORGANIZATION NAMES(S) AND ADDRESS(S)
Air Force Institute of Technology
Graduate School of Engineering and Management (AFIT/EN)
2950 Hobson Way
WPAFB OH 45433-7765 DSN: 785-3636

8. PERFORMING ORGANIZATION REPORT NUMBER

AFIT/GE/ENG/09-08

9. SPONSORING/MONITORING AGENCY NAME(S) AND ADDRESS(ES)
Air Force Office of Scientific Research
Attn: Dr. Arje Nachman
875 North Randolph St., Suite 325, Room 3112
Arlington, VA 22203
arje.nachman@afosr.af.mil COMM (703) 696-8427

10. SPONSOR/MONITOR'S ACRONYM(S)
AFOSR/NM

11. SPONSOR/MONITOR'S REPORT NUMBER(S)

12. DISTRIBUTION/AVAILABILITY STATEMENT

Approval for public release; distribution is unlimited.

13. SUPPLEMENTARY NOTES

14. ABSTRACT

Pseudolite measurements typically contain cycle slips and other errors that can affect reliability. Past work relied on the receiver-reported signal-to-noise (SNR) value to determine whether or not a cycle slip occurred. However it has been shown that even when the SNR is relatively high, a cycle clip can occur. To reduce the error in the pseudolite measurements, the pseudolite system was integrated with an inertial navigation system (INS). The integrated system detects failures through residual monitoring using a likelihood function. Integrating the inertial sensor provides a means for a filter to maintain the reliability of the pseudolite data which, in turn, increases the integrity of the resulting navigation solution. An experiment was conducted using six pseudolites and a ground vehicle equipped with a pseudolite receiver, and both a commercial-grade and tactical-grade inertial systems. Results from this experiment have shown cycle slips in the carrier phase measurements were detected and corrected using both commercial-grade and tactical-grade INS, but that performance, in terms of probability of detection and time to detect, was improved with the higher quality inertial data.

15. SUBJECT TERMS
Pseudolites, Global Positioning System, Kalman Filtering, Residual Monitoring, Failure Detectection, Inertial Navigation

16. SECURITY CLASSIFICATION OF:			**17. LIMITATION OF ABSTRACT**	**18. NUMBER OF PAGES**	**19a. NAME OF RESPONSIBLE PERSON**
REPORT	**ABSTRACT**	**c. THIS PAGE**			Raquet, John F., Ph.D., AFIT
U	U	U	UU	116	**19b. TELEPHONE NUMBER** *(Include area code)* (937) 255-3636, ext 4580 john.raquet@afit.edu